3-2020

Laser Induced Thermal Degradation of Carbon Fiber-Carbon Nanotube Hybrid Laminates

Joshua A. Key

Recommended Citation

Key, Joshua A., "Laser Induced Thermal Degradation of Carbon Fiber-Carbon Nanotube Hybrid Laminates" (2020). *Theses and Dissertations*. 3888.
https://scholar.afit.edu/etd/3888

LASER INDUCED THERMAL DEGRADATION OF CARBON FIBER-CARBON NANOTUBE HYBRID LAMINATES

THESIS

Joshua A. Key, 1st Lieutenant, USAF

AFIT-ENP-MS-20-M-104

DEPARTMENT OF THE AIR FORCE
AIR UNIVERSITY

AIR FORCE INSTITUTE OF TECHNOLOGY

Wright-Patterson Air Force Base, Ohio

DISTRIBUTION STATEMENT A.
APPROVED FOR PUBLIC RELEASE; DISTRIBUTION UNLIMITED.

AFIT-ENP-MS-20-M-104

LASER INDUCED THERMAL DEGRADATION OF CARBON FIBER-CARBON NANOTUBE HYBRID LAMINATES

THESIS

Presented to the Faculty

Department of Engineering Physics

Graduate School of Engineering and Management

Air Force Institute of Technology

Air University

Air Education and Training Command

In Partial Fulfillment of the Requirements for the

Degree of Master of Science in Engineering Physics

Joshua A. Key, BS

1st Lieutenant, USAF

March 2020

DISTRIBUTION STATEMENT A.
APPROVED FOR PUBLIC RELEASE; DISTRIBUTION UNLIMITED.

AFIT-ENP-MS-20-M-104

LASER INDUCED THERMAL DEGRADATION OF CARBON FIBER-CARBON NANOTUBE LAMINATES

Joshua A. Key, BS

1st Lieutenant, USAF

Committee Membership:

Maj N. Herr, PhD
Chair

Dr. C. Rice
Member

Dr. M. Marciniak
Member

AFIT-ENP-MS-20-M-104

Abstract

Recent advancements in fiber laser technology have increased interest in target material interactions and the development of thermal protection layers for tactical laser defense. A significant material of interest is carbon fiber reinforced polymers due to their increased use in aircraft construction. In this work, the thermal response of carbon fiber-carbon nanotube (CNT) hybrid composites exposed to average irradiances of 0.87-6.8 W/cm^2 were observed using a FLIR sc6900 thermal camera. The camera had a pixel resolution of 640x512 which resulted in a spatial resolution of 0.394x0.383 mm/pixel for the front and 0.463x0.491 mm/pixel for the back. The hybrid samples that showed the highest absolute and relative reduction in heat penetration contained three CNT outer layers on the front and backside and one CNT center layer respectively. When compared to the 8-layer carbon fiber control sample, they demonstrated a backside peak temperature reduction of 120 ℃ and 85 ℃ respectively. This reduction in temperature appears to be due to the production of an insulating layer produced by the trapping of organic volatile gases in the CNT layers. The insulating layer reduces the through thickness thermal conductivity preventing heat conduction to the backside. Scanning electron microscope images and optical microscope images are presented that support this explanation. The introduction of CNT layers to carbon fiber reinforced composites reduced heat penetration to deeper layers preventing/delaying thermal degradation of those layers when exposed to laser irradiation.

Acknowledgments

I would like to express my sincere appreciation to my wife Katie Key for her patience and support as I completed this program, Maj Herr for all of his technical expertise relating to the chemistry and physics involved in thermal degradation of composites, Dr. Rice for all of his help in the lab and all of the equipment that he made available for the experiment, and Dr. Marciniak for helping me with radiometric concepts. I also would like to thank Stephen Shock for his work building the enclosure and cooling pump that was used in these experiments. I would also like to thank Dr. Pitz, Dr. Anderson, Mr. Guild, Mr. Stalnalker for helping me get to AFIT. Without them, I would not have made it to this point.

Joshua A. Key

Table of Contents

Page

List of Figures

Page

List of Tables

Page

LASER INDUCED THERMAL DEGRADATION OF CARBON FIBER-CARBON NANOTUBE HYBRID LAMINATES

I. Introduction

General Issue

The conceptual idea for the laser was introduced in a paper published in 1916 by Einstein detailing a derivation of Plank radiation law. In this paper Einstein A and B coefficients were introduced, and the idea that photons could be used to extract identical photons from excited atoms via stimulated emission was postulated [1]. Forty-Four years later, Theodore Maimen demonstrated the validity of Einstein’s idea by making a ruby laser at Hughes Research Labs. The invention of the laser started a technological revolution, and within six years, military interest in laser weapons led to the development of a 50 kW CO_2 laser. Despite many efforts, viable high-power laser weapon systems of this power have not been fielded [2]. However, recent advancements in fiber laser technology has created an increased interest in fielding tactical laser weapons systems. As of 2008, single mode fibers have achieved over 3 kW of power and incoherently beam combined laser systems have achieved over 90% propagation efficiencies across 1.2 km of moderate turbulence [3]. Due to this emerging threat, a large variety of materials used in aerospace applications will soon be subject to potential laser attacks. This evolving vulnerability requires a knowledge of thermal material degradation processes and material modifications that could be used to mitigate the effects of tactical laser weapon systems.

Carbon Fiber Reinforced Polymers

A significant material of interest in regard to tactical laser weapon systems is carbon fiber reinforced polymers (CFRPs) due to their increased use in aircraft for their high specific strength, stiffness, and customizability [4]. The thermal degradation process of CFRP materials is complex. Heating via laser irradiation initiates degradation processes that cause spatial and temporal evolution of material properties including emissivity, thermal conductivity, and heat capacity of the material. Additionally, the material undergoes a variety of endothermic decomposition reactions, with the release of volatile organic products. These organic volatiles cause surface combustion of carbon fiber composite materials under piloted ignition or laser heated self-ignition. This surface combustion contributes exothermically to the degradation process and can ignite regions in which organic volatiles' temperature has not reached critical temperatures [5]. These complexities make it difficult to model the thermal evolution of composite systems and have historically pushed high energy laser lethality testing to rely on data supported empirical models [6].

The test matrix for this strategy is exceedingly large, due to the large number of materials, laser properties, and various engagement parameters that can be investigated. However, using thermal cameras, temporal and spatial temperature measurements of CFRP material undergoing degradation can be used to constrain models and allow for the estimation of unknown parameters such as the reaction rates and activation energy for the endothermic reactions [5]. Herr et al; demonstrated the validity of this approach by modeling the thermal degradation of carbon fiber epoxy composite material, using known/measured material properties and thermal imagery collected using a FLIR SC6000

MWIR camera. Their model showed the temperature dependence of multiple CFRP breakdown mechanisms, which indicates that a reduction in temperature could preserve material properties and potentially maintain function in response to tactical laser attacks. One approach that has been successful in reducing thermal degradation of composite materials, is the introduction of carbon nanotube (CNT) sheets in the reinforcing phase of a composite material. The introduced CNTs achieve this reduction by providing an increased conductivity that diffuses the heat load into a larger amount of the material. The diffusion of this heat load resulted in smaller amounts of material reaching peak temperatures that exceeded thresholds for several degradation mechanisms, resulting in strength preservation and reduction in mass loss due to ablation [7-10].

Carbon Nanotubes

Due to the electron configuration of carbon, it can form a diverse variety of bond geometries resulting in many structural isomers, geometric isomers, and enantiomers. These properties also result in three solid phase allotropes: diamond, graphite, and buckminsterfullerene. In these allotropes and other molecules, covalent bonds are formed by the promotion of 2s electrons to 2p orbitals. This can occur in three different ways, one of which results in three sp^2 orbitals that are on the same plane separated by an angle of 120 degrees [11]. It was this orbital structure that Iijima observed in 1991 when investigating helical microtubes of graphitic carbon [12]. Iijima was the first to recognize that these graphene sheets had a large potential number of helicities and chiralities, and that carbon nanotubes can come in the form of single walled carbon nanotubes and multi-walled carbon nanotubes as shown in Figure 1 [13-15].

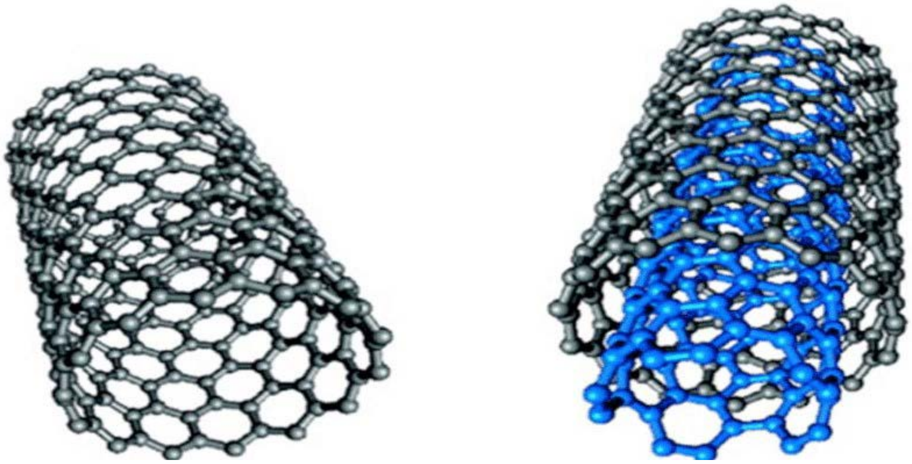

Figure 1. Single Walled Carbon Nanotube and Multi Walled Carbon Nanotube [13-15]

Since their discovery, carbon nanotubes have displayed impressive properties that motivate scientists and engineers to apply them in various applications. Carbon nanotubes have demonstrated tensile strength two orders of magnitude above steel, a melting point of 4000 K in ideal vacuum, variable electrical conductivity properties depending on atomic structure, and have some of the highest known thermal conductivity [16, 17]. However, despite achieving these properties for individual nanotubes, scientists and engineers have thus far failed to realize them in bulk materials such as yarns and sheets [15].

Problem Statement

Although bulk materials have failed to replicate the individual properties of carbon nanotubes, bulk CNT materials have shown promise in improving the thermal resistance of traditional carbon fiber composite materials [7-10]. However, the literature has little information on laser induced thermal degradation of carbon fiber – carbon nanotube hybrid laminates, so this work will investigate the thermal degradation of these materials to determine the best arrangements of carbon fiber – carbon nanotube laminates to provide superior thermal protection layers for use in directed energy defense applications.

Research Questions

To determine best arrangements, various stages of testing will be conducted on carbon fiber, carbon nanotube, and hybrid laminates to determine their individual material properties as well to identify any differing degradation mechanisms.

The first objective of this research is to characterize the thermal response of carbon fiber reinforced polymer panels, so that adequate comparisons may be made between the carbon fiber and hybrid samples. Additionally, various fiber orientations will be explored to determine the effect of fiber orientation on heat conduction in the material and subsequent thermal degradation.

The second objective of this research will be to characterize the thermal response of CNT sheets, so that differing behavior between pure CNT samples and hybrid samples may be explained using a combination of the determined carbon fiber and carbon nanotube thermal properties. Additionally, this will allow for the observation of any differing degradation mechanisms between CNT and carbon fiber break down, which should indicate which material would be a favorable top layer.

The third objective of this research is to demonstrate whether these hybrid laminates provide a benefit, and if so, what the optimal arrangements are. A summary of these objectives is shown below in Table 1.

Table 1. Summary of Research Objectives and Methodology

Research Objectives	**Methodology**
O1: Characterize Carbon Fiber Thermal Response	Expose samples to various irradiances and record thermal response
O2: Characterize Carbon Nanotube Thermal Response	Expose samples to various irradiances and record thermal response
O3: Characterize Hybrid Samples Thermal Response	Expose samples to various irradiances and record thermal response

Limitations

Air Force Research Laboratory Materials and Manufacturing Directorate (AFRL/RX) provided unused test samples that were manufactured for the characterization of mechanical and vibrational dampening properties [15]. For this reason, ideal control samples were not available. Additionally, test layups were not designed with the goal of investigating the effects of a single side asymmetric layups, or alternating layers. Conclusions based on these samples provided insight into how the materials degrade, and potentially more optimal layups are postulated. In addition to this, testing was done in a lab environment that did not support the high velocity and/or turbulent conditions that aircraft may experience. The airflow in these conditions may have the effect of carrying organic volatile byproducts away from the laser spot; resulting in a delay or prevention of self-ignited combustion contributing to the heating process. Additionally, the increased airflow would increase convective cooling, and potentially cause more stress on the surface of the material.

Preview

Future tactical laser weapons systems will likely target CFRP materials in aircraft. The addition of carbon nanotube sheets to CFRPs has been shown to increase the thermal resistance of composite materials due to their distinct thermal properties [7-10]. This research will help determine how differing arrangements of carbon fiber and carbon nanotube layers affect the thermal resistance of the material. Chapter II reviews the target materials, laser composite material interaction, heat diffusion and degradation of the materials, and the fundamentals of radiometric temperature measurement techniques. Chapter III covers the manufacturing and quality of the materials, the experimental set up, and the justification for the test matrix. Chapter IV discusses the test results and the analysis used to make the conclusions outlined in Chapter V. Chapter V also covers recommendations for future work.

II. Background

Chapter Overview

This section provides a background understanding of the production and properties of cyanate ester resin, carbon fibers, and carbon nanotubes. In addition, this chapter will cover the radiometric concepts used to measure the temperature of the samples and the irradiance profile of the beam.

Cyanate Ester Resin

Cyanate ester resins are a family of thermosetting polymers characterized by their reactive cyanate end groups ($-O-C\equiv N$) on an aromatic ring; the general structure of these monomers can be seen in Figure 2. In this structure the linkage X and substituent R can be varied to impart specific properties to the resin. This family of thermosetting monomers contains two cyanate functional groups and will homopolymerize into a polycyanurate under the presence of heat and/or a catalyst [18, 19].

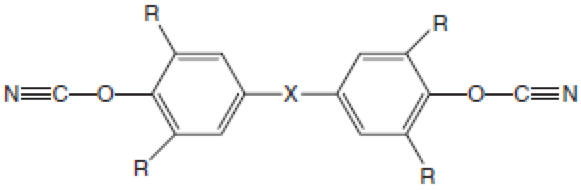

Figure 2 General structure of cyanate ester monomers where the linkage X and substituent R are chemical structures that vary across the polymer family [18].

To form polymers, the $(-O-C\equiv N)$ functionality of the monomers is cyclotrimerized through a step-growth process. The resulting polymer structure is a network of oxygen-linked triazine rings and bisphenol ethers. In this process no volatiles are produced, allowing for void-free castings that can achieve a good surface finish in fiber reinforced composites [19, 20].

Although the substituent R and linkage X may vary in the monomer structure to impart specific properties to the resin, polycyanurates exhibit similar thermal decomposition properties with decyclization of the cyanurate rings and major mass loss occurring around 450 ℃ [19,20]. The total thermal decomposition process occurs in four stages. At 400-450 ℃ random scission and cross-linking of the hydrocarbon backbone occur with no major mass loss. Above 450 ℃ the triazine rings decompose and produce a primary solid residue and the production of volatile compounds. The production of this primary residue increases with the aromatic content of the polymer and incorporates about two thirds of the nitrogen and oxygen present in the original material. This primary residue then decomposes between 500 and 700 ℃ with the elimination of alkenes and hydrogen, resulting in a carbonaceous char containing residual oxygen and nitrogen. The amount of char produced is proportional to the glass transition temperature and/or carbon bond unsaturation of the monomer [20]. Thermal decomposition during gasification may contribute to microcracking and delamination in the composite. This potentially can be exacerbated by the vaporization of unreacted catalyst. The vaporized unreacted catalyst struggles to diffuse through the resin network’s tight molecular structure resulting in the creation of delaminated voids in the material. An example of this was observed by Chung et al; who postulated the vaporization of unreacted catalyst as the mechanism for delamination in carbon fiber cyanate ester laminate material. This can be seen in Figure 3 [21].

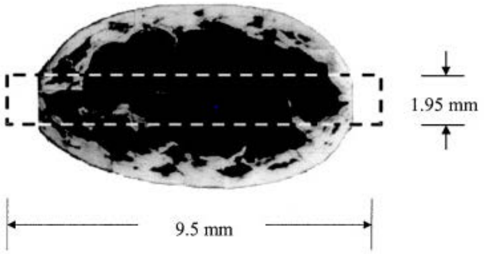

Figure 3. Void created by the vaporization of unreacted catalyst in a cyanate ester carbon fiber composite [21].

Carbon Fiber

Due to their high specific strength, carbon fibers have been increasing in demand for use in aerospace, military and other applications. Carbon fibers contain greater than 90% carbon by mass, and they are obtained through pyrolysis of an appropriate precursor material. Two economically viable precursors are acrylic and pitch [22]. Commercially 90% of carbon fibers have polyacrylonitrile (PAN) precursors due to their superior carbon yield and the carbon fibers' resulting tensile and compressive properties [22-24]. Due to this, the formation of carbon fibers through the pyrolysis of PAN-based fibers are the subject of this review.

Polymer chains can be formed from a single monomer or a set of comonomers. Polymer chains formed from a single repeating monomer unit is called a homopolymer, and polymer chains formed from more than one species of monomer (comonomers) are called copolymers. PAN polymer product is produced in several ways; however, the most common method of PAN precursor production is aqueous dispersion of acrylonitrile and selected comonomers and polymerization via a free radical mechanism. Homopolymer PAN products are not used for the production of carbon fibers due to the rapid release of heat. The rapid release of heat causes chain scissions due to thermal shock in the resulting PAN fibers decreasing the modulus of the fiber and subsequently the eventual carbon fibers. Comonomers can hinder this heat release by slowing the exothermic reactions resulting in higher quality fibers. Additionally, comonomers assist the stabilization process, improve mobility of the polymer chains, reduce the initiation temperature of cyclization, and impart variations on carbon fiber properties. Common comonomers include methyl acrylate, carboxylic acids, acrylamide, and sodium acrylate. Of these comonomers, acrylonitrile and methyl acrylate are considered the ideal pair due to their similar polarity, resonance, and stearic hinderance [25].

PAN-based fibers can be produced from these polymer products using a variety of spinning materials and processing conditions yielding different carbon fiber material properties. Variable processing conditions include dope concentration (monomer concentration in solution), temperature, extrusion rate, coagulation bath temperature, PH, washing and stretching bath temperatures, as well as drying temperature [23]. Typically, wet spinning techniques are used to produce most PAN-based carbon fiber precursors; however, it is slowly being replaced by dry jet wet techniques [24,25]. The resulting chemical structure of the PAN fibers can be seen in Figure 4 [22].

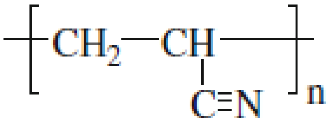

Figure 4. Chemical structure of PAN-based precursors [22]

After spinning, the PAN-based fibers undergo a variety of heating and chemical processes to yield carbon fibers. First, the PAN-based fibers are thermally stabilized in air by a low temperature heat treatment at around 200-300 ℃ to prevent melting or fusion of the fibers in subsequent processes. In this process, the linear molecules of the PAN-based fibers are converted to a cyclic structure [22]. This can be seen in Figure 5.

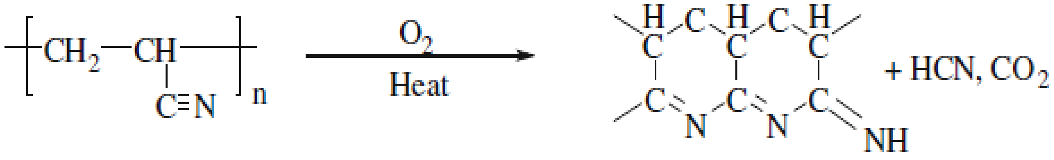

Figure 5. Conversion of the linear structure of the PAN-based polymers to a cyclic structure [22].

This process is followed by carbonization, the removal of hydrogen and nitrogen, and graphitization, the rearrangement of carbon into graphitic structure, of the fibers in an inert atmosphere to yield hexagonal graphitic structures, seen in Figure 6. This two-step process can be achieved with a variety of temperatures ranging from 1500-3000 ℃ depending on the eventual purpose of the carbon fibers. Higher temperatures yield a higher degree of carbonization and graphitization, and a subsequently higher elastic modulus. In temperatures higher than 2000 ℃, argon must be used instead of nitrogen, due to the production of cyanogen in carbon nitrogen reactions [22].

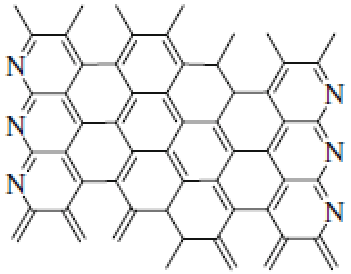

Figure 6. Resulting graphitic structure after carbonization and graphitization [22].

At this point, the carbon fibers have formed with the desired mechanical properties. However, they need to undergo surface treatment to improve eventual composite bond strength between the fiber-matrix interface of the eventual composites. The specifics of these processes are largely proprietary and specific to the purpose of the carbon fibers, but common surface treatments consist of liquid or gaseous oxidation of the fibers. This can double composite shear strengths with only a 4-6% reduction in fiber tensile strength by improving bond strength between the fiber and the matrix phase [22]. Fibers produced from this whole process normally have a tensile modulus from 200 to 350 GPa, strength from 3 to 7 GPa, and thermal conductivity < 14 W/mK [24]. The overall process is summarized in Figure 7.

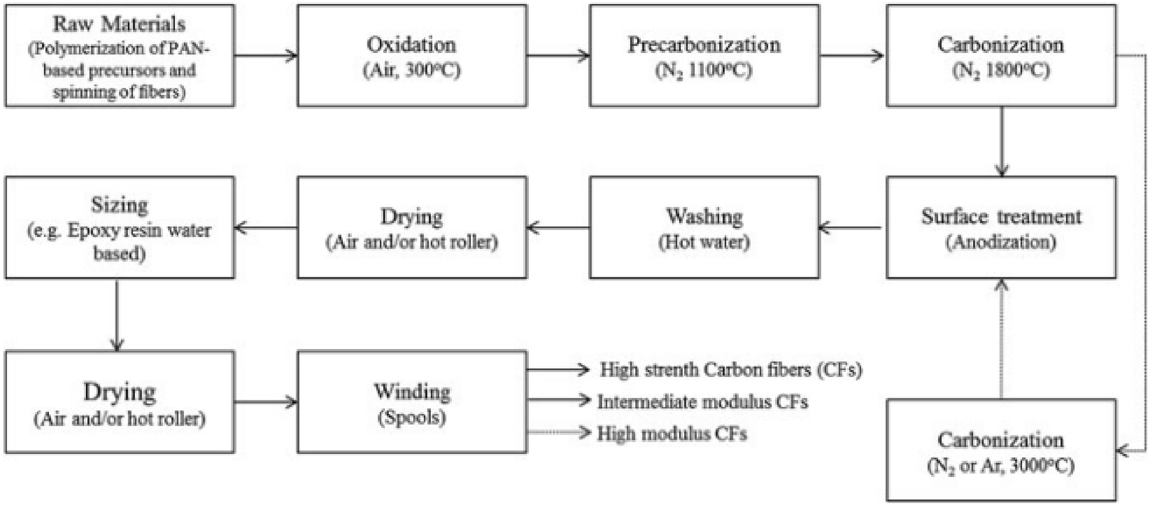

Figure 7. Manufacturing process of carbon fibers from PAN-based precursors [22].

The large number of variables in the manufacturing process results in a wide range of attainable thermal properties in carbon fibers. Differing precursor material and heat treatment temperatures can change thermal conductivity and heat capacities [26].

Carbon Nanotubes

In their simplest description, carbon nanotubes are sheets of graphene rolled into a tube. CNTs were first produced by Iijima using an arc discharge technique in 1991. Since then, catalytic chemical vapor deposition (CVD) and laser ablation techniques have emerged.

The arc discharge technique produces CNTs by passing direct current through graphite electrodes in close proximity with each other. This method typically produces multi walled carbon nanotubes (MWCNTs), which are made up of multiple concentric single walled nanotubes. Single walled carbon nanotubes (SWCNTs) can be produced by incorporating a metal catalyst on the graphite anode or cathode.

In the laser ablation technique, a mixture of graphite and metal catalysts in a hot furnace is vaporized by a pulsed or continuous wave laser to produce $C_3, C_2,$ and C. These low weight molecular species condense and form SWCNTs with the help of the metal catalyst vapors. There have been no reports of the production of MWCNTs using this technique. Unlike the arc discharge technique, the laser ablation technique would produce no CNTs without the presence of metal catalysts [27].

The bulk CNT material used in this work was produced using catalytic CVD methods. The general strategy to produce CNTs using CVD methods is to flow hydrocarbon gases, commonly ethylene or acetylene, with an inert gas in a tube reactor at approximately 550 to 750 ℃. At these temperatures, the hydrocarbons decompose and deposit carbon on catalyst material supported by alumina [27].

The most common catalyst materials used for CVD are iron, cobalt, and nickel. The carbon precipitates into carbon nanotubes due to its low solubility in these metals. In this scheme, carbon nanotubes can grow in a tip growth mode, where carbon nanotubes grow from an iron particle down, or a base growth mode, where carbon nanotubes grow from an iron particle up. In this method carbon nanotubes form over other allotropic materials because it requires the lowest amount of energy [27].

This technique has two variations that have made significant progress: fixed bed & fluidized bed. In the fixed bed method SWCNT or MWCNT production can be controlled by using different substrates. Additionally, substrate/CNT interaction governs the alignment and type of CNT production. In the fluidized bed method, there is a large available surface area for CNT growth and great temperature uniformity. Due to this, industry has mostly been using the fluidized bed technique for large scale production [27].

Produced carbon nanotubes can have a variety of chiralities that modify atomic structures and impart unique properties to individual carbon nanotubes [17]. The different atomic structures can be described by the chiral vector and the chiral angle defined as

$$C_h = n\vec{a}_1 + m\vec{a}_2 \tag{1}$$

$$\theta = \frac{m\sqrt{3}}{2n + m} \tag{2}$$

where n and m are integers and $\vec{a}_1$ and $\vec{a}_2$ are unit vectors 2.46 angstroms in length. The variable chiralities are depicted in Figure 8.

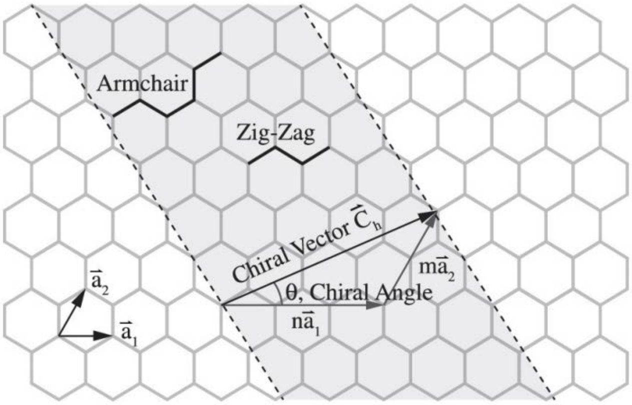

Figure 8. Diagram of graphene sheet depicting the chiral vector and chiral angle, as well as the resulting cases for the minimum and maximum chiral angle [28]. The dotted line indicates the edge of the roll.

The unique roll of the CNT tube is described by the chiral index (*n*, *m*). The three general configurations of the atomic structure are armchair, zigzag, and chiral (seen in Figure 9) corresponding to chiral indices of (*n*, *n*), (*n*,0), (*n*, *m*) respectively [27].

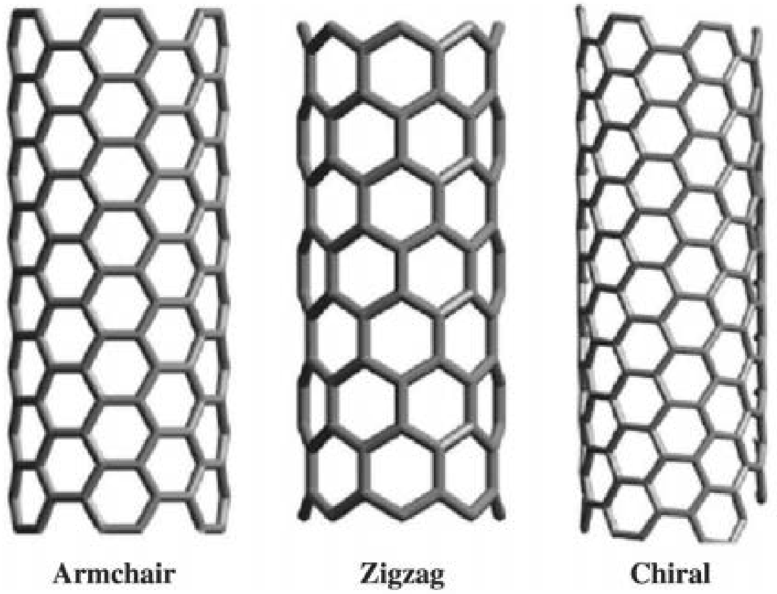

Figure 9. CNT structures corresponding to chiral vectors (n, n), (n,0), (n, m) respectively [29].

Depending on an individual SWCNT's chiral index (*n*,*m*), it can be classified as either a metallic or semi-conducing material. If the difference in *n* and *m* is a multiple of three then the carbon nanotube is classified as metallic, otherwise it is semi-conducting. Due to the multiple layers and individual chiralities in MWCNTs, SWCNTs have more distinctive electrical and optical properties [27].

Theoretically, individual SWCNTs can have an anisotropic thermal conductivity in the tube direction of $k = 6000\ W/m\ K$ making them appealing for heat management applications. Unfortunately, large assemblies of carbon nanotubes have to be assembled to achieve the desired heat flow. In these large assemblies, bulk CNT materials exhibit thermal conductivities on the order of 50 $W/m\ K$. This reduction in thermal conductivity is due to phonon mode suppression within MWCNTs and sheet imperfections such as nanotube interconnections (conduction from one tube to another) and nanotube misalignment [31].

Laser Composite Material Interaction

Heating of composite materials exposed to laser radiation is largely determined by the scattering and absorption mechanisms of the individual composite components. Bulk optical properties are determined by a combination of the absorption, reflectance and transmittance of the individual materials and the structure of the composite material.

Epoxy in carbon fiber/epoxy composites is largely transparent to near IR so laser light incident on the surface is either diffusively or specularly reflected, transmitted and scattered to deeper fibers, or absorbed. The primary absorbers in these composite materials are the carbon fibers, with an absorptivity of 0.78 for normal incidence. The absorptivity of these carbon fibers is further enhanced due to the effect of multiple inter-material scatterings that give transmitted light more opportunities to be absorbed by adjacent carbon fibers [32]. This behavior is depicted in Figure 10.

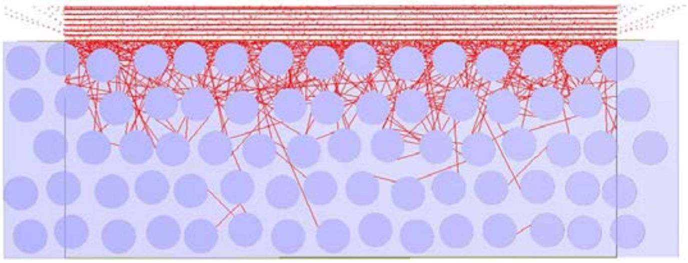

Figure 10. Ray propagation through composite material. The horizontal lines represent scattered light from the epoxy surface, while dotted lines represent light scattered out of the material [32].

The result is an overall material absorptivity that is greater than either the carbon fiber or epoxy absorptivity, which for carbon fiber/epoxy composites has been measured at 0.93 at a wavelength of $1.3\mu m$. Additionally, the scattering of light off of the carbon fibers to neighboring carbon fibers causes almost complete absorption in the first few fiber layers and an intense amount of energy concentration at the surface contributing to a steep temperature gradient in the material [32].

It is for similar reasons that CNT sheets, also known as “buckypapers”, have large absorptivities, and vertically aligned SWCNT forests have demonstrated some of the highest and spectrally wide absorptivities ever measured [33]. A plot comparing the different emissivity of bulk carbon nanotube structures can be seen in Figure 11. By Kirchhoff’s law, which states that an object’s emitted radiation must equal its absorbed radiation at thermal equilibrium, Figure 11 shows the approximate absorptivity of the material. For this reason, it is expected that samples with carbon nanotube sheet top layers will absorb similarly, but not identically to the carbon fiber controls.

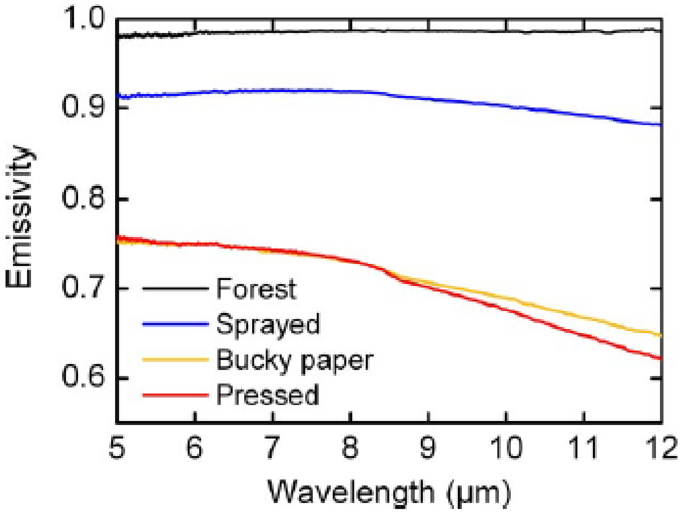

Figure 11. Emissivity of various CNT structures [33].

Theoretical Description of Thermal Degradation

As laser irradiation is absorbed by carbon fibers and conducted to the surrounding polymer matrix, it initiates rapid heating, potentially causing degradation of the material. This thermal response is similar to the thermal response of CFRP materials exposed to fire. The heat introduced in both cases decomposes polymer and fiber materials producing volatile gases, solid carbonaceous char, and smoke. The main difference between laser irradiated decomposition and fire induced decomposition is that laser irradiated heating does not ignite organic volatiles until sufficient surface temperatures of 1150 °C are reached [5]. Due to this similarity many models for the decomposition of CFRP materials in a fire may be applied to laser irradiated heating with the subtraction or delay of any exothermic terms that model the combustion and heat contributions of the organic volatiles [5, 34].

To aid understanding of the resulting theoretical model, the terms will be introduced according to the chronology of the thermal decomposition of carbon fiber reinforced polymers. Under the presence of a one-sided heat flux, heat is initially conducted through the material described by the diffusion equation

$$\rho C_p \frac{\partial T}{\partial t} = k_x \frac{\partial^2 T}{\partial^2 x} + k_y \frac{\partial^2 T}{\partial^2 y} + \ k_z \frac{\partial^2 T}{\partial^2 z} \tag{3}$$

where ρ is density, C_p is heat capacity, and k is thermal conductivity of the material with boundary conditions

$$k \frac{\partial T}{x, y, z} = \ - h(T - T_\infty) - \bar{\epsilon}\sigma(T^4 - T_\infty^4) + \alpha(\lambda)L \tag{4}$$

where k is thermal conductivity, h is the convection coefficient, $\bar{\epsilon}$ is the average emissivity, σ is Stefan-Boltzmann's constant, $\alpha(\lambda)$ is the absorptivity of the material at the laser wavelength λ, and L is the laser irradiation. T is the surface temperature of the composite, and T_∞ is the ambient temperature of the environment. In this work, k_x and k_y will be considered in-plane thermal conductivities, and k_z will be considered through plane or though thickness conductivity. The bulk composite thermal properties depend on both the thermal conductivity of the carbon fibers and the resin matrix. In carbon fibers the thermal conductivity can vary from 20-80 W/mK, while in resins it can vary from 0.10 to 0.25 W/mK. Due to this, heat absorbed in the fibers is quickly conducted in the fiber direction, while slowly conducted through the polymer matrix to the adjacent fibers, resulting in steep temperature gradients. This can be complex to model, because $k, C_p, \bar{\epsilon}, \alpha(\lambda)$ change with temperature, decomposition, and sometimes wavelength. These changes require the individuality of the material properties at different points in the material will have to be accounted for [34].

As the CFRP material heats up to 100-150 ℃, moisture in the resin matrix begins to vaporize creating dehydrated regions in the resin. Further heating to 400-450 ℃, in cyanate esters, initiates random scission and cross linking of the hydrocarbon backbone of the polymer with no major mass loss. Above 450 ℃ the triazine rings break down producing primary solid residue and volatiles [19,20]. This production of gaseous material struggles to permeate through the polymer matrix which can result in high internal gas pressures, measured up to ~10 atm in laminates, which can produce pores, delaminations and matrix cracks [34]. These decomposition processes are endothermic and have a cooling effect on sample. The release of heated gases also marginally cools the sample by carrying away heat from the sample. This is largely determined by the heat capacity of the individual molecules, the mass flow rate, and the amount of vaporized, escaping material.

The cooling effect of these processes will depend on the heat of the reaction, reaction rates, and the amount of reactants in the composite material. The reaction rates for these reactions can be modeled using an Arrhenius kinetic rate equation

$$\frac{\partial m}{\partial t} = -A_i m_o \left[\frac{m - m_f}{m_o}\right]^{n_i} e^{-E_a/RT} \tag{5}$$

which models the reaction rate as a function of the unreacted population above the activation energy. In the equation above, A_i, E_a, and n_i are the pre-exponential factor, activation energy, and order of the reaction respectively. The variables m_o, m_f, and m are the initial, final and instantaneous mass of the reactant material.

By modeling the reaction rates, the heat equation can be modified with the addition of multiple Arrhenius decomposition terms depending on the individual polymer breakdown process, and the heat loss due to the convective flow of vaporized hot gases.

$$\rho C_p \frac{\partial T}{\partial t} = k_x \frac{\partial^2 T}{\partial^2 x} + k_y \frac{\partial^2 T}{\partial^2 y} + k_z \frac{\partial^2 T}{\partial^2 z} + \Sigma \frac{Q_{rxn}}{V} \frac{dm_{rxn}}{dt} + \frac{C_{p,gas} \partial T}{V} \frac{dm_f}{dt} \qquad (6)$$

In this equation, the endothermic reactions are accounted for by the heat of the decomposition reaction term Q_{rxn} multiplied by the reaction rate dm_{rxn}/dt. Additionally, the flow of hot vaporized moisture and organic volatiles is modeled by the last term.

The fibers are more thermally stable than the polymers in this process but they can oxidize under the presence of enough heat and atmosphere. Typically, fibers undergo a small initial mass loss in air or nitrogen over the temperature range 300-500 ℃ due to the decomposition of the organic sizing compound on the carbon fibers. At higher temperatures, 500-950 ℃, much larger mass loss occurs in the fibers due to oxidation. The oxidation of carbon fibers in composite materials is limited to the surface due to the production of organic volatile gases in the decomposing resin. The produced gases typically diffuse out of the material preventing the flow of oxygen into the composite.

This mass loss also depends on fiber diameter when heated in air. The oxidation reaction of the fibers can be accounted for with an additional Arrhenius reaction term in the heat equation [35]. Similar to the carbon fibers, carbon nanotubes initially thermally oxidize at 520 ℃ with a maximum mass loss at 650 ℃ [36].

Radiometric Temperature Measurement

Every object in nature is an absorber and emitter of radiation. When an object thermally emits at the theoretical max, it is called a blackbody and has an emissivity $\epsilon(\lambda, T) = 1$ at all wavelengths and temperatures. Perfect emitters do not exist, but very close approximations can be made by creating a small aperture in the wall of an isothermal enclosure. If the enclosure is large (dimensions ≫ wavelengths), then the emitted radiance from the small aperture will not depend on the geometry of the enclosure and will obey the relation:

$$L_\lambda(\lambda, T) = \frac{2hc^2}{\lambda^5} \frac{1}{e^{\frac{hc}{\lambda kT}} - 1} \quad \left(\frac{W}{cm^2\, \Omega\, \mu m}\right) \tag{7}$$

where h is Planck’s constant, c is the speed of light, λ is the wavelength, k is Boltzmann’s constant, and T is temperature. Cavities can achieve this approximation because any light externally incident on the cavity is either reflected and trapped in the cavity (if the aperture is small) or absorbed and reradiated by it. In this sense, a small aperture to a large isothermal enclosure is a perfect absorber because it does not allow externally incident light to escape, resulting in blackbody radiative behavior. This is the fundamental upper limit for thermal radiation that no object can supersede. Due to this, the description of how well objects emit radiation is defined by the ratio between the source exitance and blackbody exitance.

$$\epsilon(\lambda, T) \equiv \frac{M_\lambda(\lambda, T)|_{source}}{M_\lambda(\lambda, T)|_{blackbody}} \tag{8}$$

With the emissivity defined as the ratio between the source exitance and the exitance of a true blackbody, the thermally emitted radiance of non-blackbodies can be described by the equation

$$L_{\lambda, Object} = \epsilon(\lambda, T) * L_\lambda(\lambda, T) = \epsilon(\lambda, T) * \frac{2hc^2}{\lambda^5} \frac{1}{e^{hc/\lambda kT} - 1} \tag{9}$$

where the source radiance is just the blackbody radiance times the source emissivity. This does not account for all of the radiance emitted from an objects surface. The total radiance in the case that $\epsilon < 1$ also contains the reflected radiance from the ambient environment. In cases where this radiance is small this term may be ignored. By using this relationship, thermal cameras can be calibrated to measure the temperature of objects based purely on their emitted radiation. This is achieved by observing approximate blackbodies with emissivities very close to 1 at a variety of temperatures. The calculated radiance of these blackbodies at landmark temperatures is then correlated to the measured response of the detector to build a relationship between detector response and radiance and by extension, temperature. Once this correlation has been established, temperature can be obtained by using the measured radiance, the observation wavelength, and inverting Planck's equation to solve for temperature. It is important to note that by using spectral bandpass filters the observed wavelength can be constrained and the emissivity can be approximated as a constant. Additionally, filters will reduce the amount of reflected radiance that will be incident on the detector. In the case of hot ($T > T_\infty$) objects strongly emitting in the observation range, the reflected irradiance will be small compared to thermally emitted irradiance and can be neglected.

$$T(\lambda, L_{Object}) = \frac{hc}{\lambda k \ln(\left(\frac{L_{\lambda,Object} * \lambda^5}{2\mathrm{hc}^2 * \epsilon(\lambda,\mathrm{T})}\right)^{-1} + 1)} \tag{10}$$

Alternatively, polynomial fit functions that fit radiance to temperature within the dynamic range of the detector may be used to map measured radiance to temperature [37].

Recording temperature measurements through this technique easily allows for the high spatial and temporal resolutions from thermal imagery. Unfortunately, the range of observable temperatures is limited by the dynamic range of the detector. To circumvent this a technique called super framing may be used. Super framing allows an extension of dynamic range at the cost of temporal resolution, by collecting thermal imagery using multiple sequential integration times. This sacrifices temporal resolution to gain a dynamic range less than or equal to the sum of the ranges of the individual integration times. This allows dynamic ranges of greater than 1000 °C to be achieved.

The limitation of radiometric temperature measurement is that the accuracy of the temperature measurement will largely depend on the accuracy of the measured emissivity values which can have high spectral dependency that evolves with temperature. Spectral band pass filters can mitigate this complexity, because spectral bandpass filters only transmit observed radiation at a particular wavelength range allowing users to use emissivity measured values for a “single” wavelength. This provides less complexity in the emissivity correction at the cost of reduced signal. This can be offset by increasing integration times and subsequently reducing maximal frame rates.

Unfortunately, this does not address the temperature dependency. In situations where the emissivity is constant with respect to true temperature, then the correction may be applied and the resulting output is an accurate estimate of the true temperature. In thermally dynamic processes that modify the emissivity, the process is not as simple. As composite materials heat up decomposition occurs drastically changing the emissivity of the material. In cyanate ester resins, material decomposition begins approximately at 450°C. Once the resin is decomposed bare char remains contributing to the evolved emissivity. At higher temperatures the char oxidizes leaving bare carbon fiber further changing the emissivity [5]. Due to this codependence between emissivity and temperature, one emissivity correction to the observed radiometric temperature is insufficient to accurately capture the true temperature. When the first emissivity correction is applied, it yields a better estimate for the true temperature, which also yields a more accurate emissivity estimate for the material. To account for this, a new correction is applied with the better emissivity estimate. As better temperature and emissivity estimates are obtained, the solution converges to an accurate representation of the true temperature.

Radiometric Techniques Measuring Beam Irradiance

Due to the high irradiances that are characteristic of laser sources, direct imaging of the beam often saturates or damages focal plane array detectors. To circumvent this issue, imaging of the reflectance off a Lambertian surface may be performed. The bidirectional reflectance function (BRDF) describes the reflected radiance of a surface irradiated by a source. The BRDF function of a Lambertian surface is a constant, which means that the surface is has no specular reflection, and is a uniform diffusive reflector. An illustration of this can be seen in Figure 12.

$$f(\theta_i, \phi_i, \theta_r, \phi_r) = \frac{L(\theta_r, \phi_r)}{E(\theta_i, \phi_i)} = \alpha \tag{11}$$

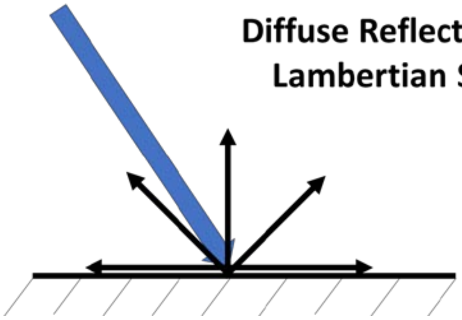

Figure 12. Diffusive reflection off of a Lambertian surface.

Due to this behavior, the reflected radiance in any viewing angle is proportional to the exitance incident on the Lambertian surface.

$$L_{reflected} \propto \; E_{inc}(\theta, \phi) \tag{12}$$

As a result, irradiance measured by focal plane array of a camera observing the reflection will be proportional to the irradiance of the beam, excluding aberrations due to atmospheric transmission and optics. This yields a relative irradiance profile that is proportional to the beam profile. By using a calibration target and power measurements, the relative irradiance profile can be spatially adjusted and scaled with power to get the irradiance profile of the actual beam [38,39].

Summary

Absorption of laser radiation in carbon fiber-carbon nanotube composite materials is largely due to the constituent material properties and composite geometry. As heating occurs, the polymer goes through a series of degradation processes that ultimately result in depolymerization and charred material. Additionally, carbon fibers oxidize at 500-950 ℃,but this is largely confined to the surface due to the production of organic volatiles. These processes can be monitored using radiometric temperature techniques and modeled using a heat equation modified with convective heat flow and endothermic Arrhenius reactions. Additionally, the irradiance profile can be captured by imaging the laser light scattered from a Lambertian surface.

III. Methodology

Chapter Overview

The purpose of this chapter is to detail the manufacturing processes used to produce the investigated composite materials, and the irradiation procedures and measurement techniques used to initiate and study the thermal decomposition of the laminate materials. The composite materials were prepared by AFRL/RX and a material quality analysis was done by 1Lt James O'Keefe.

Test Subjects

The composite materials were manufactured using carbon fibers, carbon nanotubes, and cyanate ester resin. The carbon fibers are polyacrylonitrile (PAN) based HexTow HM-63 carbon fibers manufactured by Hexcel Corporation of Stamford, Connecticut, USA. These carbon fibers have undergone additional surface treatment and the application of sizing to improve interlaminar shear strength and handling characteristics. The resulting fibers were combined in tows of thousands of individual fibers and impregnated with PMT-F6 cyanate ester resin by Patz Materials and Technologies, Benicia California, USA to form unidirectional prepreg tape. The carbon nanotubes were produced by Nanocomp Technologies of Concord, New Hampshire, USA in the form of a non-woven sheet material. The sheet material was produced by chemical vapor deposition and is composed of bundled carbon nanotubes hundreds of microns thick and millimeters long. These sheets were then treated using Patz Material resins system to create homogenous directional flow of CNTs within the sheet. The matrix phase of these composites was a toughened cyanate ester resin PMT-F6 produced by Patz Materials and Technologies [15].

The laminates were constructed using standard layup techniques by 1Lt James O'Keefe and 1Lt Casey Keilbarth. To build the laminates used in the experiment, the required laminate material was cut from the CF prepreg tape and the CNT sheets. To build the test laminates, these plies were then individually stacked together, using a technique called booking, in groups of four on a 20-psi vacuum table for 15 mins. The resulting groups were then booked together to achieve the laminate layups outlined in Table 2. The carbon fiber laminates were composed of 20 plies of unidirectional carbon fiber in the 0, 90, and 45-degree orientation. The carbon nanotube laminates were composed of 20 plies of homogenous flow CNTs in the 0, 90, and 45-degree orientation. The hybrid samples had a control sample, and three sub groups. The control sample for the set of hybrid samples contained eight carbon fiber plies in alternating 0-degree and 90-degree orientations. The subgroups contained the same carbon fiber plies, with the addition of various CNT layers. In the first subgroup (sample 3.2-3.4), CNT layers were added to the center. In the second subgroup (sample 3.5-3.8), CNT layers were added to the edges and the center in various amounts. In the final subgroup (sample 3.9-3.12), three CNT layers were added to the surface with varying amounts of CNT layers added in the center. The results of these subgroups are similar and grouped in this manner in subsequent sections. All booked laminates were then frozen to prevent resin degradation [15].

Table 2 Test Samples and Orientation. In the hybrid samples (3.1-3.12), the carbon fiber layers are in alternating 0,90-degree orientations, and the CNTs are in the 0 orientation [15].

Test #	Orientation
1.1	[0CF]20
1.3	[90CF]20
1.5	[45CF]20
2.1	[0CNT]20
2.2	[90CNT]20
2.3	[45CNT]20
3.1	[0; 90]4S
3.2	[0,90,0,90,CNT,90,0,90,0]
3.3	[0,90,0,90,CNT,CNT,90,0,90,0]
3.4	[0,90,0,90,CNT,CNT,CNT,90,0,90,0]
3.5	[CNT,0,90,0,90,CNT,90,0,90,0,CNT]
3.6	[CNT,0,90,0,90,CNT,CNT,90,0,90,0,CNT]
3.7	[CNT,CNT,0,90,0,90,CNT,90,0,90,0,CNT,CNT]
3.8	[CNT,CNT,0,90,0,90,CNT,CNT,90,0,90,0,CNT,CNT]
3.9	[CNT,CNT,CNT,0,90,0,90,90,0,90,0,CNT,CNT,CNT]
3.10	[CNT,CNT,CNT,0,90,0,90,CNT,90,0,90,0,CNT,CNT,CNT]
3.11	[CNT,CNT,CNT,0,90,0,90,CNT,CNT,90,0,90,0,CNT,CNT,CNT]
3.12	[CNT,CNT,CNT,0,90,0,90,CNT,CNT,CNT,90,0,90,0,CNT,CNT,CNT]

Once all of the panels were assembled, they were thawed for layup and curing. The layup sequence from bottom-to-top on the mold surface was: release film (Kapton sheet), non-porous Teflon, laminate, porous Teflon, non-porous Teflon, bleeder cloth (x2), and vacuum bagging as shown in Figure 13. Additionally, edge dams were used to prevent excessive resin bleeding [15].

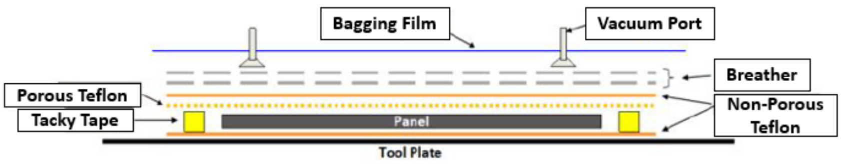

Figure 13. Stacking sequence of materials for autoclave processing [15].

The assembly was then vacuum-bagged under full vacuum to expel air at 26 psi. Leak checks showed that the bag leaked less than 0.5 psi/min. All composites were then cured by an autoclave using the PMT-F6 curing procedures by the manufacturer. The procedure was: ramp up 5 °F /min to 220 °F under vacuum bag pressure, dwell 220 °F for 30 mins at 80 psi autoclave pressure, ramp 5 °F/min to 350 °F, maintain 350 °F for 4 hours, ramp down 5 °F/min to room temperature and remove pressure. An overview of this process can be seen in Figure 14. To ensure laminate quality, four thermocouples were placed in the laminate layers to provide autoclave feedback during the cure cycle [15].

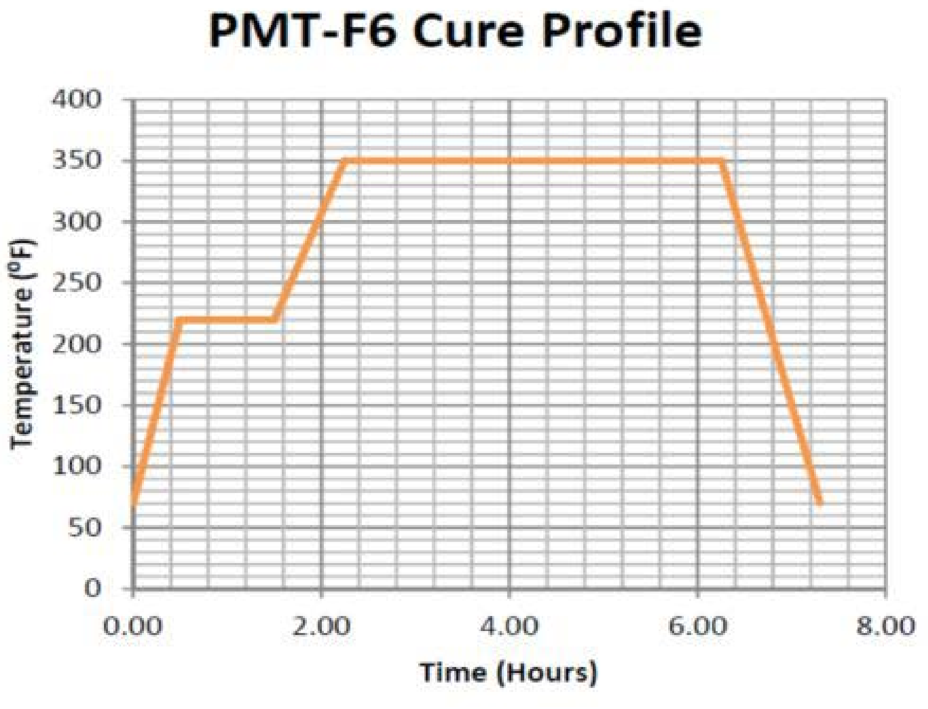

Figure 14. The temperature ramps and settings used to cure the PMT-F6 cyanate ester resin in the laminate material [15].

After curing was complete an ultrasonic C-scan was performed by AFRL/RX on a Wesdyne system to determine if there were any areas of delamination, matrix or fiber cracking, and resin rich or resin starved areas. An example of the results can be seen below in Figure 15. The uniform color in Figure 15 indicates that no delamination or matrix cracking occurred test sample 3.3. Similar scans indicated that the other test samples were also free of delamination and matrix or fiber cracking [15].

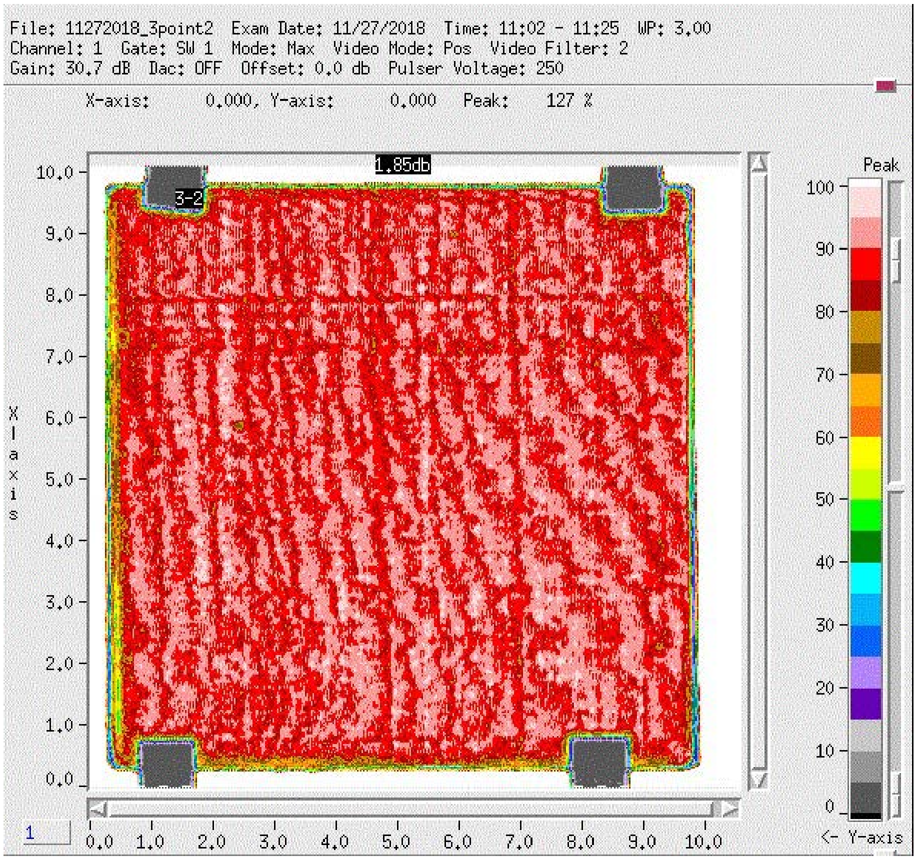

```
File: 11272018_3point2  Exam Date: 11/27/2018  Time: 11:02 - 11:25  WP: 3.00
Channel: 1  Gate: SW 1  Mode: Max  Video Mode: Pos  Video Filter: 2
Gain: 30.7 dB  Dac: OFF  Offset: 0.0 db  Pulser Voltage: 250
        X-axis:      0.000, Y-axis:      0.000   Peak:    127 %
```

Figure 15. Ultrasonic C-scan of test sample 3.2. The image uniformity indicates no delamination or matrix cracking [15].

Once quality was assured, the AFIT Model shop cut the test samples according to the dimensions shown in Figure 16, resulting in the sample dimensions outlined in Table 3. The samples' volumetric dimensions were determined using a caliper gauge with a resolution of 0.01 mm. Sample dimensions were measured in three locations on each sample and then averaged to get the final result. The mass of the samples was measured three times and averaged with a Voyager Pro scale with a resolution of 0.0001 g. The lengths of the samples are not reported at this point because the samples were further cut using a diamond tipped hacksaw in preparation for laser irradiation testing. The lengths of individual samples varied and will be reported with the report of the individual test results [15].

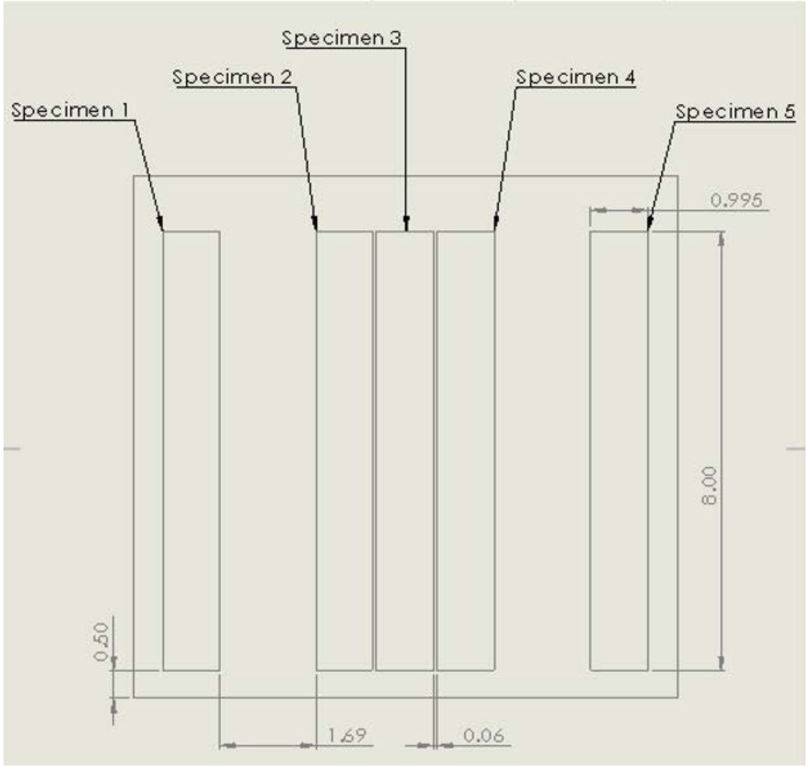

Figure 16. Individual Test Specimens cut from a single laminate [15].

Table 3. Summary of material dimensions and densities [15].

Test #	Avg Thickness (cm)	Avg Width (cm)	Volumetric Density (g / cm^3)
1.1	0.224±0.002	2.539±0.001	1.535±0.013
1.3	0.235±0.001	2.537±0.002	1.544±0.010
1.5	0.235±0.005	2.537±0.002	1.537±0.024
2.1	0.066±0.004	2.531±0.001	1.349±0.034
2.2	0.064±0.004	2.532±0.002	1.347±0.050
2.3	0.067±0.002	2.534±0.002	1.370±0.021
3.1	0.094±0.002	2.534±0.002	1.518±0.015
3.2	0.101±0.005	2.534±0.002	1.492±0.058
3.3	0.105±0.000	2.536±0.004	1.498±0.013
3.4	0.105±0.001	2.536±0.003	1.500±0.021
3.5	0.108±0.001	2.532±0.002	1.484±0.006
3.6	0.112±0.001	2.534±0.002	1.466±0.024
3.7	0.115±0.001	2.534±0.002	1.469±0.018
3.8	0.117±0.002	2.534±0.003	1.469±0.023
3.9	0.119±0.002	2.533±0.002	1.450±0.018
3.10	0.120±0.003	2.532±0.002	1.478±0.018
3.11	0.123±0.002	2.534±0.004	1.487±0.030
3.12	0.125±0.002	2.535±0.000	1.483±0.022

Additional to the ultrasonic C-scan, the machined samples underwent an X-ray CT scan on a XT-H-225-ST Microfocus X-ray system to determine the porosity of the laminates. If porosity pockets existed in the material, then black dots would appear in the image. A representative of the results can be seen in Figure 17, demonstrating the lack of porosity in test sample 2.1. Similar results were found for the other samples [15].

Figure 17. X-ray CT scan of test sample 2.1. The lack of black dots indicates the lack of porosity in the material [15].

Beam Images and Power Measurements

The laser samples were irradiated with (23) 30 W (max power) Shark laser diodes that were fiber coupled into an array that directed the beams to the target samples. The set up used can be seen below in Figure 18. To characterize the irradiance profile for modeling of the experiment in future work, power and beam profile measurements were recorded pre-experiment using a UP55C-2.5kW Gentec power meter and an Allied Vision Manta G-609 B visible camera. Laser power output measurements were taken across the range of laser input currents that would be used in the experiments to irradiate the sample. The primary measured powers were 5.45, 8.19, 14.17, 25.22, and 40.75 Watts at 11.5,12,13,14,15 Amps respectively.

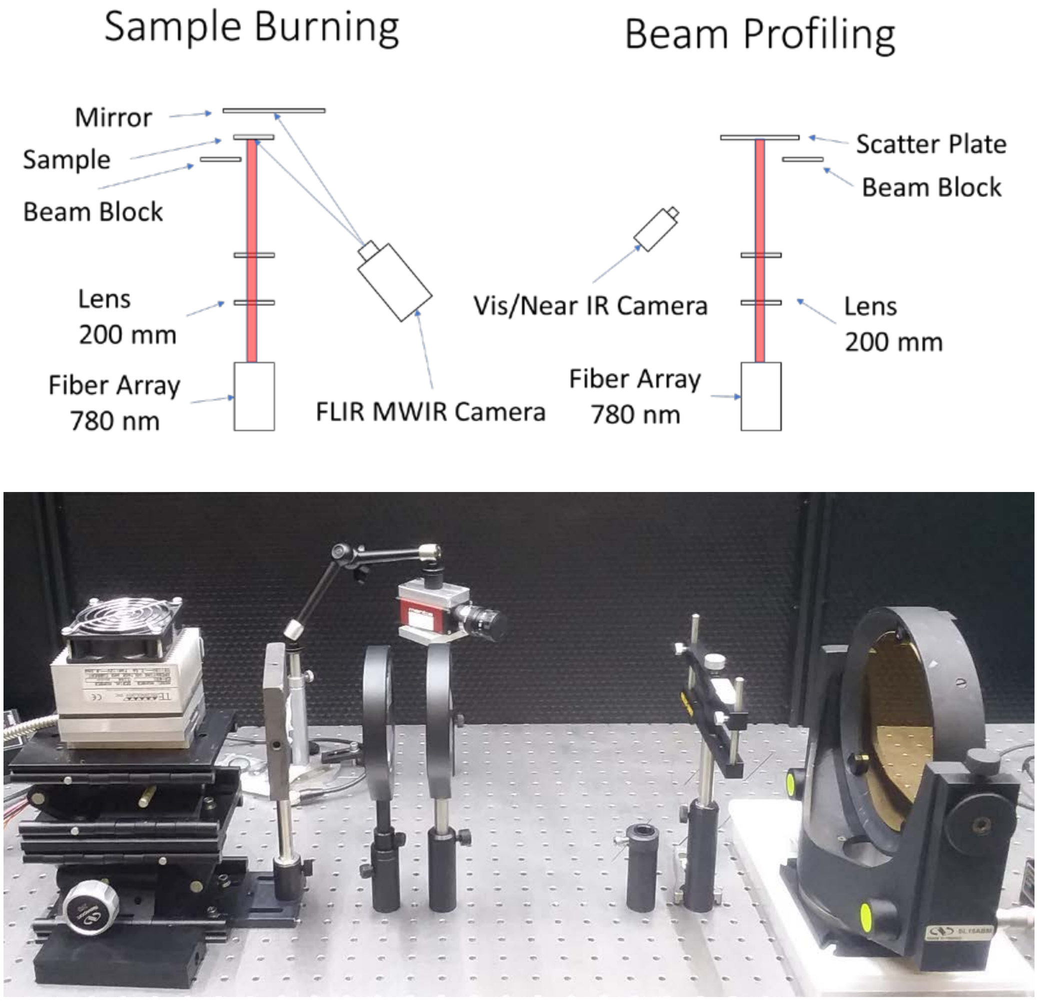

Figure 18. Diagram of Experimental setup (top) and actual setup (bottom) used to irradiate samples. Objects left to right: fiber array with cooling tower, Thorlabs optics f = 200 mm, Allied Vision Manta G-609 B visible camera, sample mount, gold plated mirror

Beam images were taken using an Allied Vision Manta G-609 B visible camera with 2752x2206 pixel resolution, and a Labsphere Spectralon reflectance reference target surface in the location of the sample mount pictured above. Beam images were taken at exposure times 3000 – 5000 microseconds. Noise frames were also taken in which the image of the scene was taken without irradiance of the Spectralon surface. These noise frames were used to do a background subtraction and distinguish signal from noise. Pixels that were less than the average background noise plus five standard deviations were zeroed, so noise data was not scaled with the power. The camera had a spectral bandpass filter at 760 nm and a 3.0 ND filter to prevent noise from other sources and saturation. The beams were spatially calibrated using a Thorlabs NBS 1963A resolution target. The spatial resolution was found to be 0.067 x 0.049 mm^2 per pixel. These resolutions were not equal due to the projection of the observed surface on the focal plane array at a non-normal viewing angle.

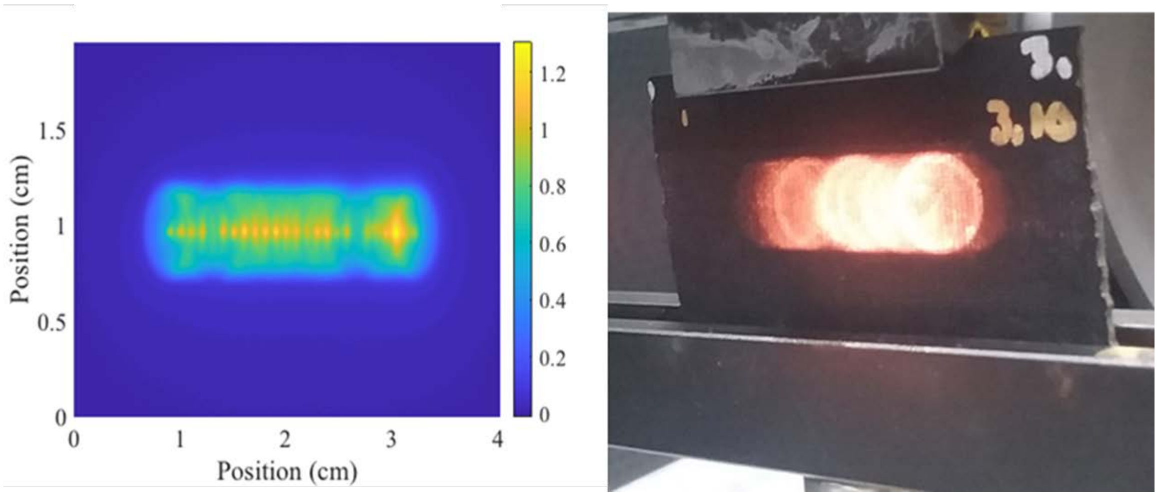

Figure 19. Left: Normalized Beam Profile, Right: Actual Beam incident on a 3.10 test sample.

The relative pixel intensity of the beam profile was converted to a relative spatial intensity profile by dividing pixel values by the pixel area. The relative intensity profile was then normalized so that the relative intensity, seen in Figure 19, integrated to 1. The normalized beam profile was then multiplied with the power measurements to yield the corresponding irradiance profiles for the experiments. An example of this can be seen below in Figure 20. Beam profiles taken at different laser powers indicated that the variations in the beam profile across power and time were not significant enough to affect modeling on a 30x30x8 mesh grid.

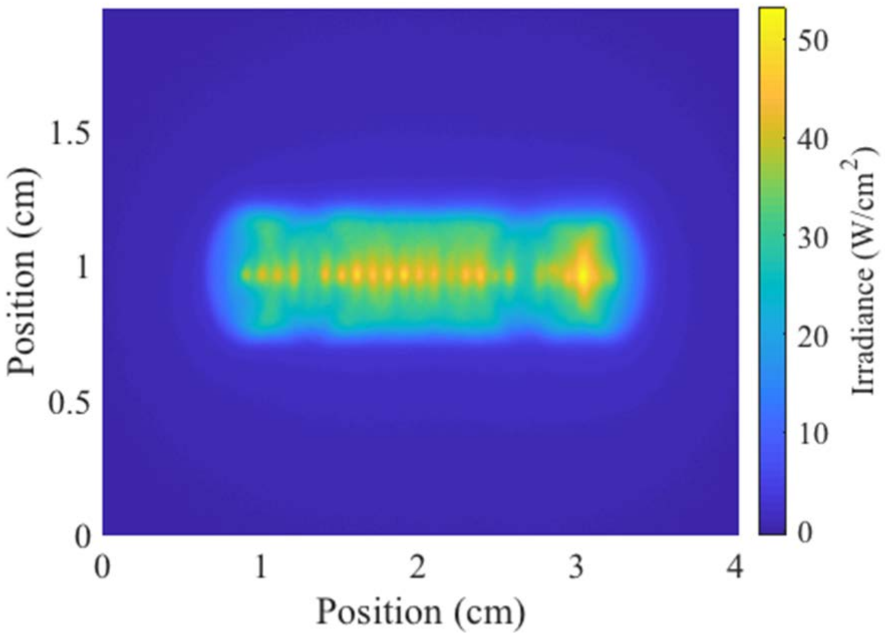

Figure 20. Irradiance profile of 40.75-watt beam from a linear array of 23 diodes. The average irradiance was 6.48 $\mathrm{W/cm^2}$, and the peak irradiance was 53.31 $\mathrm{W/cm^2}$

Experimental Set Up

The thermal imagery in this work was collected using a FLIR X6900sc MWIR camera that had a 50 mm lens and a 3.8-4.0-µm bandpass filter. The camera used an InSb 640 x 512 element detector array. The thermal responses of the samples were primarily collected at 3 Hz, however 15-Hz, and 30-Hz frame rates were used for some samples. Collection at 3 Hz was used to reduce file size and speed up processing; the temporal resolution of 15 and 30 Hz also did not provide additional information. Spatial resolution was measured to be 0.394 mm/pixel in the x direction and 0.383 mm/pixel in the y direction for the front and 0.463 x 0.491 mm^2/pixel for the back. These spatial resolutions were determined with the known dimensions of the sample in the thermal imagery. The camera was deliberately focused to the halfway point between the front and back images of the sample. This resulted in a blurring effect that can be seen in the front and back spatial distribution curves in the results.

The camera was non-uniformity corrected using a 4181 Fluke wide area blackbody. The non-uniformity corrections (NUCs) were performed at 1.2 ms, 0.27 ms, 0.05 ms, and 0.005045 ms to correspond to data collection integration times. With the exception of the shortest integration time, the NUCs used several frames of black body radiance at temperatures near the low end and high end of their linear response curves. For 0.005045 ms, the NUC was performed using a temperature at the bottom of the linear region and at 500 ℃ (maximum FLUKE temperature). The NUCs determined the median pixel response and set the gain and offsets of the individual pixels to correct the scene to the median response. Additionally, bad pixels were detected based on flickering, responsivity, and gains greater than 1.5 or lower than 0.5. Bad pixels were replaced in the output using a two-point gradient method.

The calibration of the camera was achieved using FLIR's ResearchIR calibration software and an Electro Optical Industries cavity blackbody starting at 35 ℃ and ending at 900℃. The camera collected blackbody imagery with a NUC'd scene and recorded the average pixel response for a given radiance at a given temperature. Calibration frames were collected at room temperature, 50-500 ℃ in steps of 50 ℃, and 500, 600, 700, 850, 900 ℃ at integration times of 1.2 ms, 0.27 ms, 0.05 ms, and 0.005045 ms. The calculated radiance of these scenes was then correlated to the pixel response and linear fit functions were built. The R-squared value for these fit functions were all above 0.999. The temperature to radiance relation was then built using a 6-order polynomial to achieve the flux to temperature calibration seen in Figure 21.

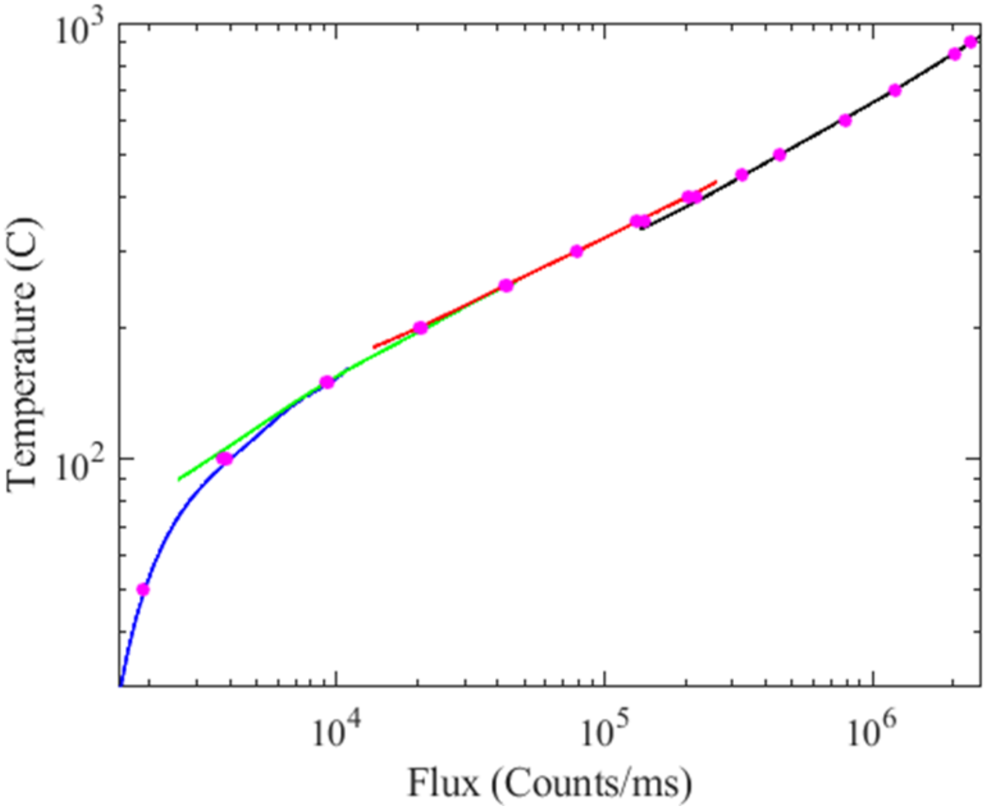

Figure 21. Calibration for all four integration times using a cavity black body. Calibrations for (-) 1.2 ms, (-), .27 ms, (-) .05 ms, (-) .005045 ms.

The NUCs and calibrations were done for multiple integration times so a dynamic range extension method known as superframing could be used. Superframing is a technique that builds a single frame out of four individual frames with different integration times. Frames within the linear region of the detector response are then averaged into one superframe allowing the user to take advantage of the range of all four integration times.

The calibration was specifically built to have overlap between the scenes, so that with superframing the camera would have a continuous dynamic range from 35-1000 ℃. The calibration suffered from some slight discontinuities between integration times resulting in some sharp, but relatively small, discontinuous jumps in the measured temperatures. The subframes were combined into one superframe by excluding the pixels outside the linear response, which was 1400-14000 counts for this detector, and then averaging the remaining valid pixels. This reduced maximal frame rates, however the sacrifice in temporal resolution only limited the maximal superframe rate to 120 Hz, which was significantly faster than the actual frame rate. The radiometric temperatures captured in these superframes were than corrected with an emissivity to obtain a true temperature measurement.

Unfortunately, the emissivity of the materials used in this work was not measured. Due to this, the applied emissivity correction is a best guess and cannot be used to make absolute statements about true temperature. The emissivity correction that was used in this work was obtained from the work of Herr et al. where the kinetics and evolving thermal properties of carbon fiber composites were investigated. In Herr et al's work, the emissivity of the material at various stages of degradation was measured and an interpolant model of the emissivity as a function of temperature was generated. For this work, this interpolant model was modified to account for the higher decomposition temperature of 450 ℃ for cyanate ester resins and can be seen below in Figure 22. Without measures of the emissivity, this model is the next best approximation. In carbon fiber composites, a large portion of the absorptivity, and by extension of Kirchhoff's law, emissivity is dependent on the carbon fibers and the geometry of carbon fiber composites. Considering these materials have this in common, temperature corrections from this emissivity model should be close to the true temperatures of the samples. The carbon nanotube surface samples may have a larger deviation from this model, so direct comparisons between carbon fiber sample temperatures and carbon nanotube surface temperatures cannot be made great confidence. Despite this, conclusions made between same surface samples, and conclusions made about the relative temperature evolution of the samples should be considered accurate depictions of the evolving temporal behavior in thermally degrading laminates exposed to laser irradiation.

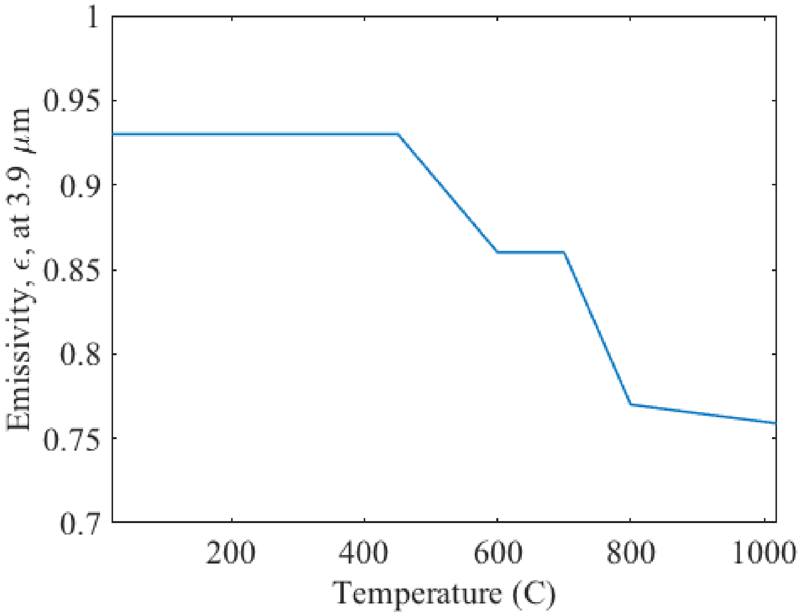

Figure 22. The interpolant model of the temperature dependence of emissivity at 3.9 μm. used to make corrections to observed radiometric temperatures.

Using this model, an iterative correction to the emissivity may be used to gain better and better estimates of the true temperature. In this work temperature-emissivity iterations were continued until a fractional difference between iterations of .1% was achieved. This typically took 5 iterations or less for the radiometric temperature to converge to the best estimate of the true temperature. The rapidity of convergence can be seen in Figure 23, and the change in the temperature estimate between iterations can be seen in Figure 24. It should be noted that in Figure 24 the temperature changes are plotted on a log scale, so in locations where convergence was achieved immediately, the plot does not display a value.

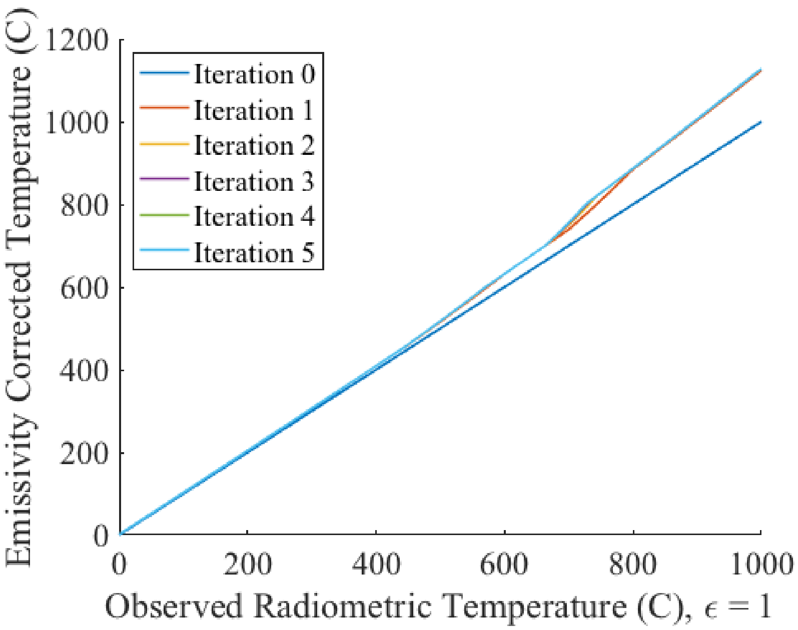

Figure 23. Iterations of radiometric temperature until convergence to the best true temperature estimate. Iteration 0 is assuming the emissivity is 1 at all temperatures.

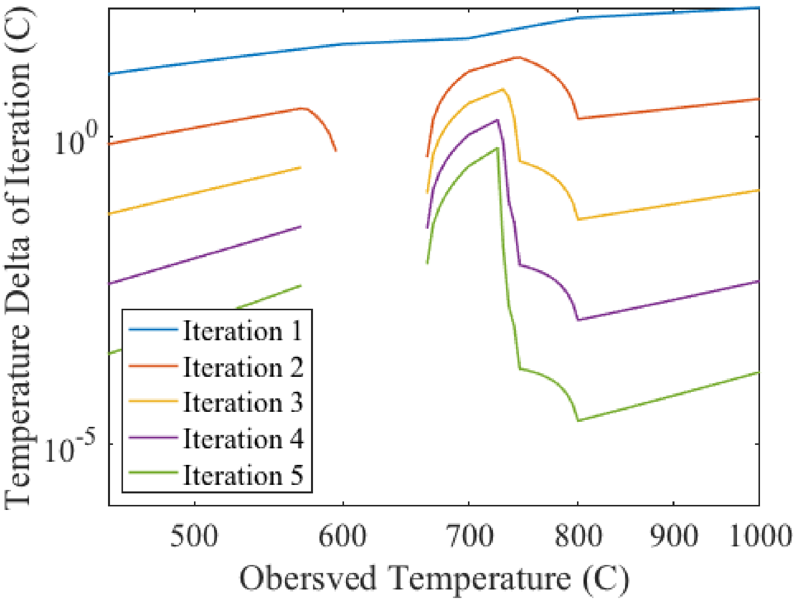

Figure 24. Change in temperature between iterations. As iterations progress the temperature changes become increasingly small, eventually converging to the best estimate for the true temperature, and the true emissivity at that temperature. In cases where the convergence is immediate, the change between iterations is zero and is not plotted on the log plot.

Considering that this model was measured for carbon fiber epoxy composites, there is an unknown uncertainty in the temperatures reported in this work. To provide some clarity, perturbations of the interpolant model emissivity is presented in Figure 25. These perturbations demonstrated that an uncertainty in emissivity of ± .3 corresponded with an uncertainty in true temperature of ± 213℃ and ± 9.1℃ at 1000 ℃ and 100 ℃ respectively, and an uncertainty in emissivity of ± .07 corresponded with a true temperature uncertainty of ± 46.21℃ and ± 2.89℃ at 1000 ℃ and 100 ℃ respectively. A more detailed depiction of this is plotted in Figure 26. It should be noted that the emissivity for the ± .3 perturbation never exceeded 1, so at maximum the upper limit on the emissivity perturbation was + .25.

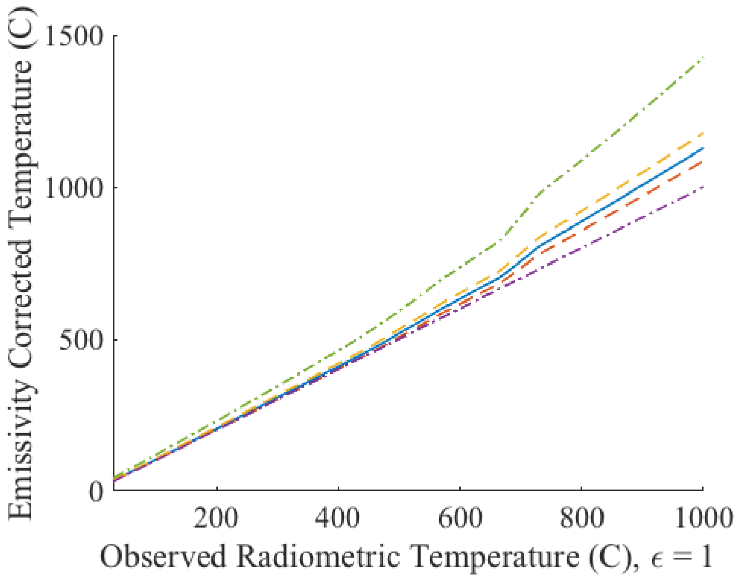

Figure 25. Different estimates of the true temperature obtained using perturbations of the interpolant model. From top to bottom, (-.) $\epsilon_{model} - .3$, (--) $\epsilon_{model} - .07$, (--) ϵ_{model}, (--) $\epsilon_{model} + .07$, (--) $\epsilon_{model} = 1$. The solid blue line was the correction used in this work.

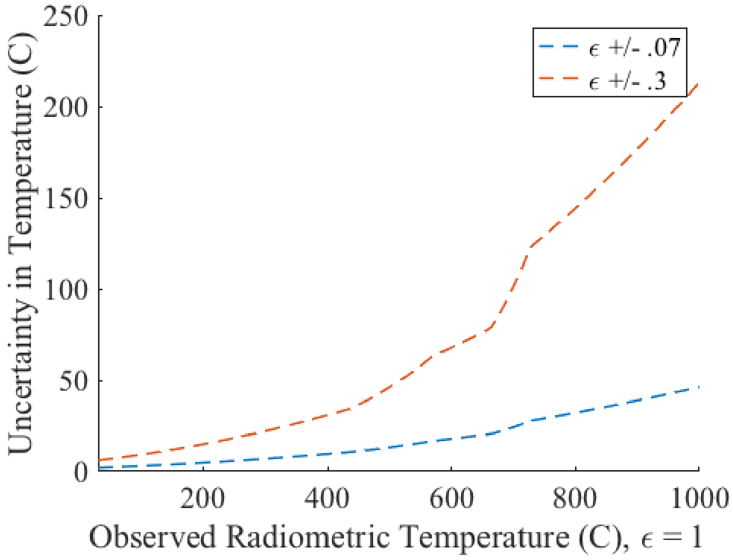

Figure 26. Uncertainty in Temperature obtained by perturbing the interpolant model by $\epsilon \pm .07$ and $\epsilon \pm .3$. It should be noted the emissivity never exceeded 1.

Test Matrix

The carbon fiber, carbon nanotube, and hybrid laminates were irradiated by a diode stack of (23) 30 W narrow linewidth laser diodes centered at a wavelength of 780 nm. Except for sample 1.1, all samples were irradiated with increasing irradiance levels until thermal degradation was observed. The average irradiance steps were 0.87, 1.30, 2.25, 4.01, 6.48 W/cm^2. These corresponded with peak irradiances in the beam profile of 7.13, 10.72, 18.53, 33.00, 53.31 W/cm^2. This was done to estimate through-thickness thermal conductivity of the material at different degradation stages, and to acquire more tests with fewer samples. Laser exposure was limited to 90 seconds and cool-down was recorded for greater than 90 seconds. A summary of the tests done can be seen in Table 4 below.

Table 4. Summary of irradiation tests

	0.87 W/cm^2	1.3 W/cm^2	2.25 W/cm^2	4.01 W/cm^2	6.48 W/cm^2
1.1					X
1.3	X	X	X	X	X
1.5	X	X	X	X	X
2.1	X	X	X	X	X
2.2	X	X	X	X	
2.3	X	X	X	X	X
3.1	X	X	X	X	X
3.2	X	X	X	X	X
3.3	X	X	X	X	X
3.4	X	X	X	X	X
3.5	X	X	X	X	X
3.6	X	X	X	X	X
3.7	X	X	X	X	X
3.8	X	X	X	X	X
3.9	X	X	X	X	X
3.10	X	X	X	X	X
3.11	X	X	X	X	X
3.12	X	X	X	X	X

Summary

The composite materials are composed of PAN-based carbon fibers, carbon nanotubes produced via chemical vapor deposition, and cyanate ester resin material. The laminates produced were free of matrix or fiber cracking, delamination, and resin variations. Additionally, an X-ray CT scan demonstrated a lack of porosity in the laminates. The thermal imagery was captured using a FLIR X6900sc MWIR camera with an InSb focal plane array. The camera had a pixel resolution of 640x512 which resulted in a spatial resolution of 0.394 x 0.383 mm^2/pixel for the front and 0.463 x 0.491 mm^2/pixel for the back. NUCs were performed for each integration time using a Fluke wide area black body. The camera was calibrated using an Electro Optical Industries cavity blackbody. Calibration frames were collected at room temperature, 50-500 ℃ with 50 ℃, and 500, 600, 700, 850, 900 ℃ at integration times of 1.2 ms, 0.27 ms, 0.05 ms, and 0.005045 ms. The radiometric temperatures were then iteratively corrected using an interpolant model of the emissivity evolution of the sample. To aide emissivity corrections, a spectral bandpass filter from 3.8-4 μm was used. A gold-plated mirror was used to simultaneously observe back side temperature measurements. Beam profiles were taken using an Allied Vision G-609B camera and a Labsphere Spectralon surface. Power measurements were taken using a 2.5 kW Gentec power meter. Tests were performed at a variety of irradiances to observe the laminate thermal response and estimate thermal properties at different temperatures.

IV. Results and Analysis

Chapter Overview

The purpose of this chapter is to report and analyze the results of the irradiation of various composite materials. Figures illustrating sample damage and thermal response are provided in two types. The first type for each sample shows the hottest pixel in the scene and the temperature evolution that that location on the sample experienced under irradiance. The second figure shows the x and y distribution of the surface temperatures with the hot pixel at the center. The hot pixel was not always the center of the sample, so the distribution is sometimes asymmetric in these graphs. This is due to the asymmetry in the beam profile, and variable alignment of the samples.

Carbon Fiber Laminate Results

The orientation of the carbon fibers relative to the beam profile had a significant effect on the conduction of heat throughout the composite and the degree of degradation of the sample. Sample 1.1 had a fiber direction that was parallel to the long axis of the beam, sample 1.3 had a fiber direction orthogonal to the long axis of the beam, and sample 1.5 had a fiber direction 45 degrees from the long axis. This resulted in significantly different distributions of the heat load, and resulted in significant change in how much of the composite volume reached degradation temperatures which can be seen in Figure 27.

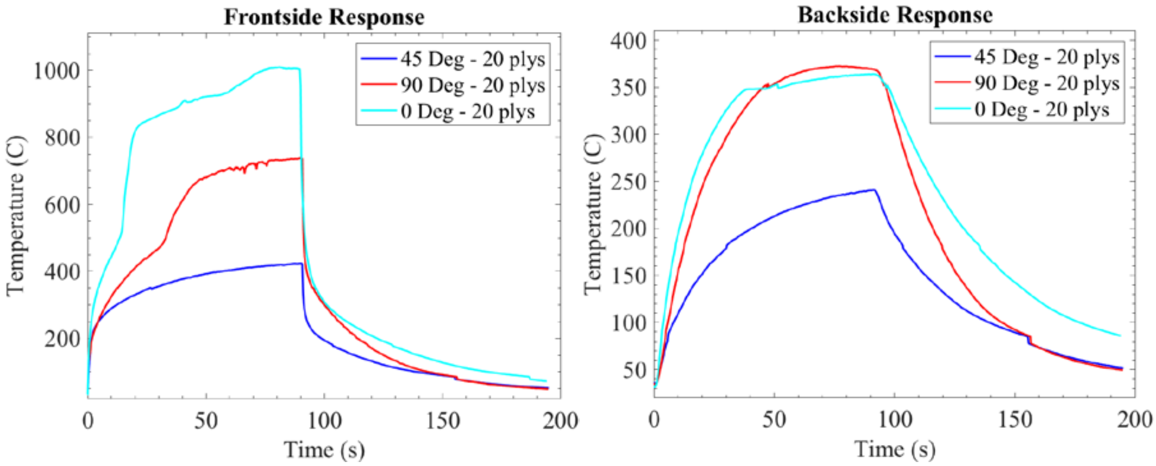

Figure 27. Thermal response of the average hottest pixel when the carbon fiber samples were exposed to an average irradiance of 6.48 $W/\ cm^2$, Sample 1.1-0° (--), 1.3-90°, (--), 1.5-45° (--)

In sample 1.1, the beam was incident on the fewest number of fibers resulting in a concentrated absorption of heat in those few fibers. This resulted in large thermal gradients in a high conductivity fiber direction and the rapid conduction of heat to the edges of the sample in the x direction, and the slow diffusion of heat out of these concentrated fibers into the surrounding polymer material due to the much lower polymer matrix thermal conductivity. This caused a large concentration of heat in the resin around these fibers and consequently higher temperatures on the front and backside. Diffusion of the heat through the composite in the through thickness direction, mostly through resin material, distributed the heat fairly uniformly in the x direction on the backside. The resulting damage can be seen in Figure 28 and the spatial distribution of the heat can be seen in Figure 29. The backside had not quite reached steady state, however it seemed to be approaching 370 °C.

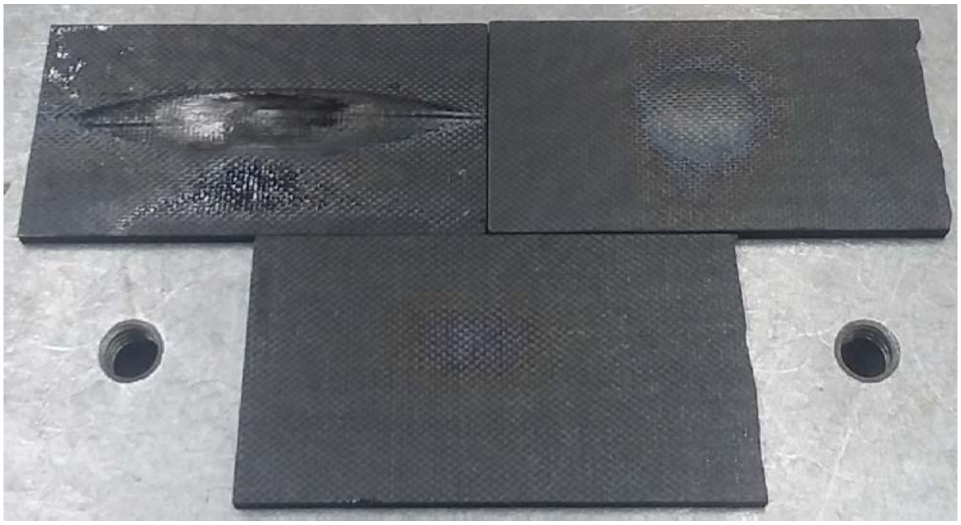

Figure 28. Top Left, sample 1.1 with fibers along the long axis of the beam. Top right, sample 1.3 with fibers orthogonal to the long axis of the beam. Bottom, sample 1.5 with fibers 45 ° to the long axis of the beam.

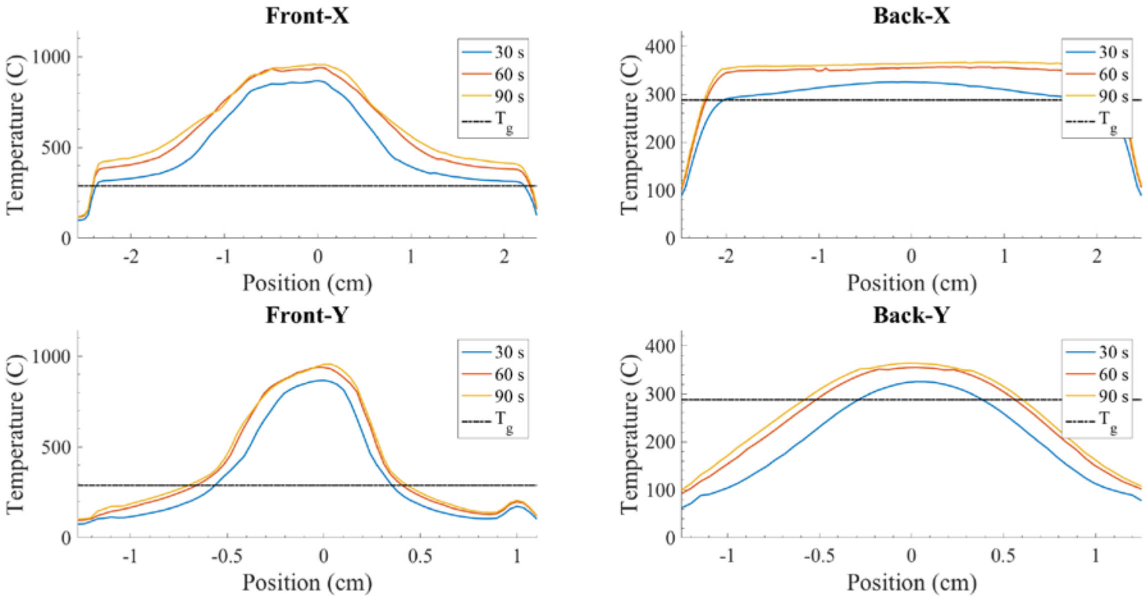

Figure 29. The spatial distribution of the heat in sample 1.1 (0 degree Orientation) when exposed to an average irradiance of 6.48 W/cm^2. (--) 30 secs, (--) 60 secs, (--) 90 secs. The horizontal line is the glass transition temperature of 288 ℃.

In sample 1.3 the fibers were oriented at 90 degrees to the long axis of the beam resulting in the absorption of the radiation into a larger number of fibers. This resulted in rapid heat conduction to the edges in the y-direction and the diffusion of the heat to a larger volume of the sample. This larger diffusion allowed more of the sample to reach a higher temperature, but reduced the volume that reached the decomposition temperature threshold. The differences between the diffusion directions can be seen in Figure 30. Most notably, the y-direction experienced a relatively uniform distribution of heat due to the higher conduction of heat along the fibers compensating for the asymmetric beam profile. This sample reached frontside steady state temperatures of approximately 750 ℃ and backside steady state temperatures of 380 ℃.

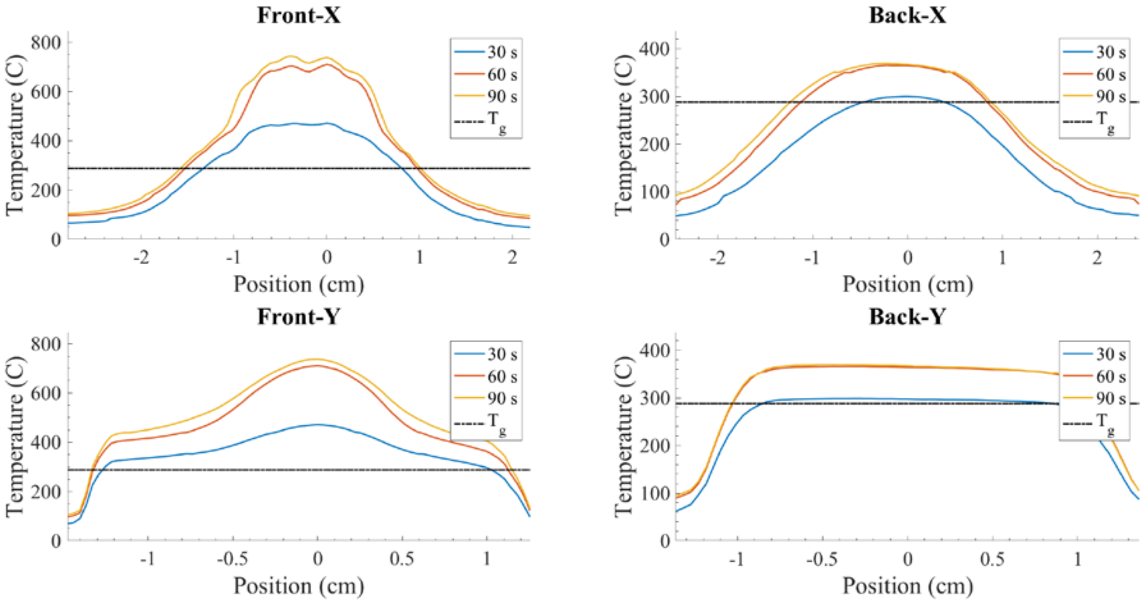

Figure 30. The spatial distribution of the heat in sample 1.3 (90-degree orientation) when exposed to an average irradiance of 6.48 W/cm^2. (--) 30 secs, (--) 60 secs, (--) 90 secs. The horizontal line is the glass transition temperature of 288 ℃.

The largest reduction in heating of the backside and subsequently deeper layers, was sample 1.5, with fibers running at a 45-degree angle to the long axis of the beam. Sample 1.5 increased the number of fibers absorbing incident laser energy (relative to the 0 deg orientation), but it also had the benefit of having more fiber volume than the sample in 1.3. In sample 1.3 the fibers could conduct heat over 1.269 cm of fiber before reaching the edges of the sample. However, in sample 1.5 this was increased by a factor of 1.414. This had the effect of making more of the composite volume available for quick heat distribution. This can be seen in Figure 31, which compares the case of sample 1.1, 1.3, and 1.5.

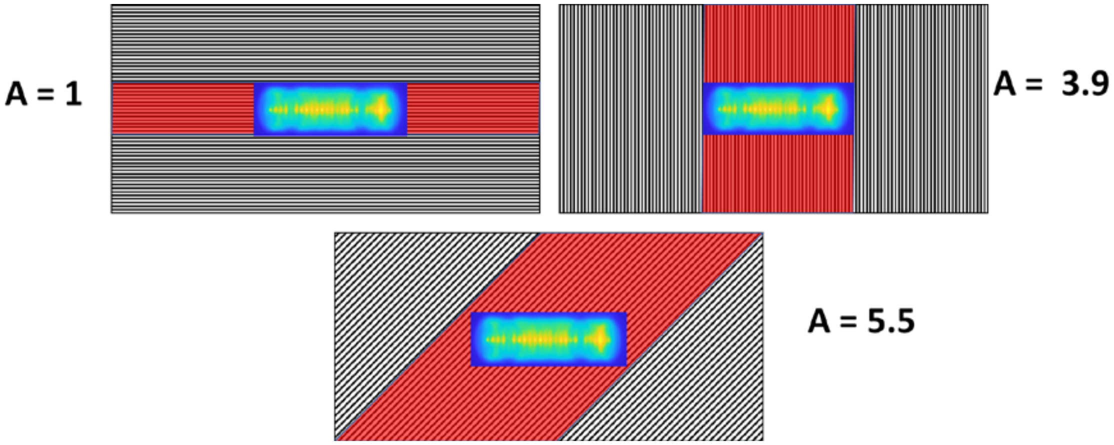

Figure 31. Sample 1.1 can quickly conduct heat to the area depicted by the thin rectangle illustrated top left. Sample 1.3 can quickly conduct heat to the thick rectangle depicted top right, sample 1.5 can quickly conduct heat across the parallelogram depicted bottom. Sample 1.3 and Sample 1.5 have a factor of 3.9 and 5.5 more material to effectively conduct heat to. In large scale structures, the edges will be at "infinity" and the areas of the top left and bottom shapes will be roughly equal.

The overall result of this additional reachable thermal mass was a reduction in frontside and backside hot pixel steady state temperature and a more even distribution of heat load on the backside which seen in Figure 32. This sample had the least damage of the three, which can be seen above in Figure 28. It should be noted that the edges in these tests were not at "infinity," and that this is a small-scale behavior that should not scale to large bulk materials. If the edges had been at infinity, the fibers in 90-degree and 45-degree orientations with respect to the beam long axis would have effectively the same access to the bulk composite material resulting in more similar behavior. The samples with fibers in the 0-degree orientation would still see some detrimental effect because they absorb the heat in fewer fibers bottling heat up at the center.

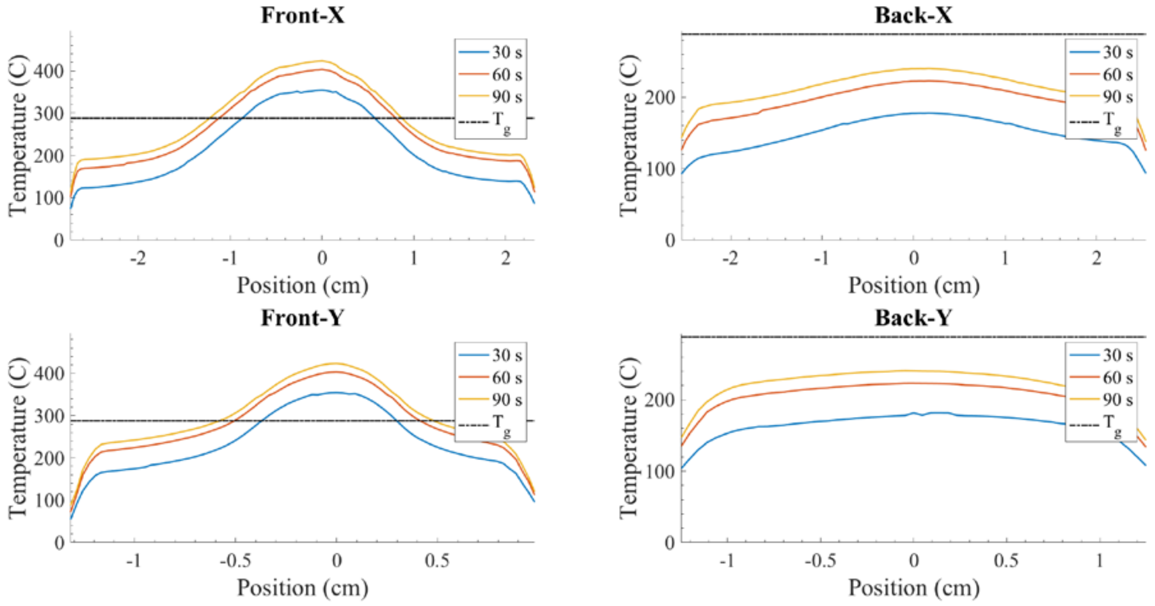

Figure 32. The spatial distribution of the heat in sample 1.5 (45 degree orientation) when exposed to an average irradiance of 6.48 W/cm^2. (--) 30 secs, (--) 60 secs, (--) 90 secs. The horizontal line is the glass transition temperature of 288 ℃.

Both Samples 1.1 and 1.3 exhibited degradation around 480-520 ℃, and the backsides were relatively unscathed. Only Sample 1.1 showed discoloration indicative of degradation on the backside.

Although fiber direction had the greatest effect in reducing steady state temperatures across all tests, fiber direction is largely determined by the load requirements of the individual composite structure and is not an available design parameter for thermal protection. In addition, this effect only occurred due to the beam asymmetry. If a symmetric Gaussian beam were to irradiate the samples, then the number of fibers absorbing the irradiance would be the same in all cases and subsequently the samples would behave more similarly. However, these tests effectively demonstrated how in-plane thermal conductivity can quickly and evenly distribute heat to more of the composite resulting in lower peak temperatures and less degradation of the composite.

Carbon Nanotube (CNT) Laminate Results

The CNT sheets are composed of tangled carbon nanotubes hundreds of microns thick and millimeters long that have a homogenized flow direction in the sample. They likewise absorb incoming radiation and conduct it to the surrounding matrix. However, the CNTs are smaller and have a higher packing fraction than the fibers. As a result, when the resin decomposes and produces volatile organic decomposition products, the carbon nanotube layers confine these resin decomposition products, causing gas pressures in the laminate to build up enough to cause ply delamination. This commonly happens in laminates due to gases struggling to diffuse through the tight polymer structure. In cyanate ester resins, this has been shown to produce voids in the material [21]. In these samples, it appears that this process is intensified by the CNT sheets due to their tight structure, which can be seen in Figure 33, causing extreme bubbling in the samples that can be seen below in Figure 34.

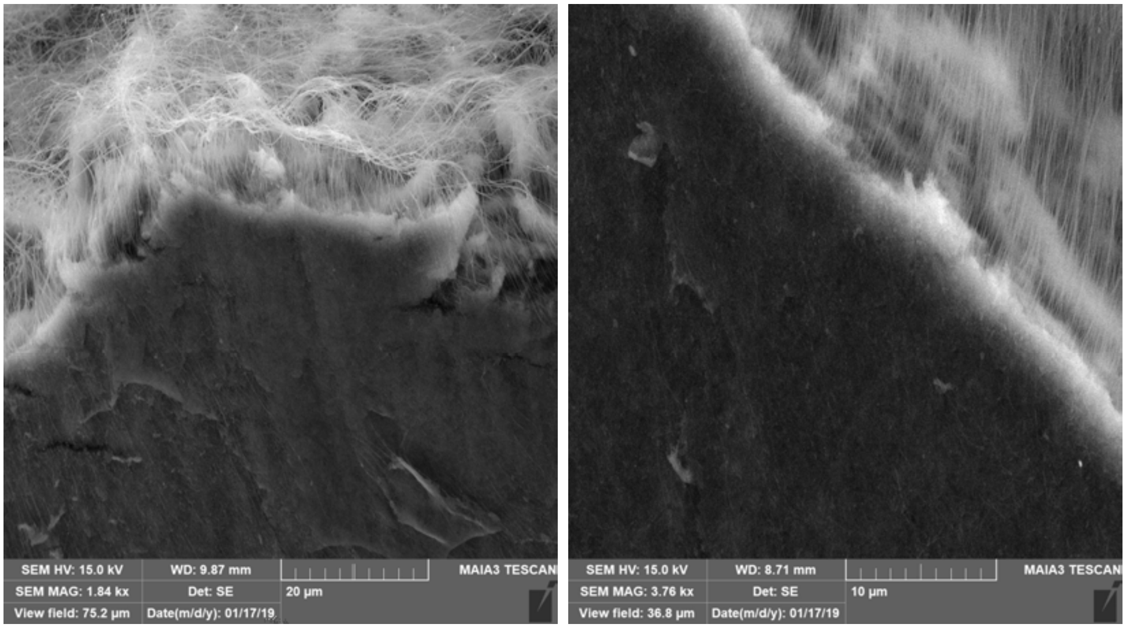

Figure 33. CNTs at the fracture surface of a 0-degree (left) magnified 1840 times and 90-degree (right) laminate sample magnified 3760 times [15].

Figure 34. Top Left, sample 2.1 nanotube alignment along the long axis of the beam. Top right, sample 2.2 nanotube alignment orthogonal to the long axis of the beam. Bottom, sample 2.3 nanotube alignment 45 ° to the long axis of the beam.

These bubbles continue to grow as the resin degrades, causing a significantly large pressure buildup in the material. The thermal conductivity of the decomposition gases is very low and this layer significantly reduces the through-thickness conductivity in this region. This leads to rapid frontside heating as the conduction pathway into the material has effectively been cut off. The rate of oxidation of the CNT increases at these higher temperatures. As the carbon nanotubes degrade and the pressure continues to build up in the laminate, eventually structural failure is induced in the carbon nanotube sheet.

This failure results in a sudden, audible release of organic volatiles causing momentary sparks and a short duration flame. An image of one of the failure sites of sample 2.3 (20 plys, 45°) can be seen in Figure 35. The damage is somewhat obscured by the production of rust from the remaining iron catalyst in the carbon nanotube sheets. An x-ray fluorescence spectrum was taken to confirm the presence of iron (in addition to the bright red coloration) and is shown below in Figure 36.

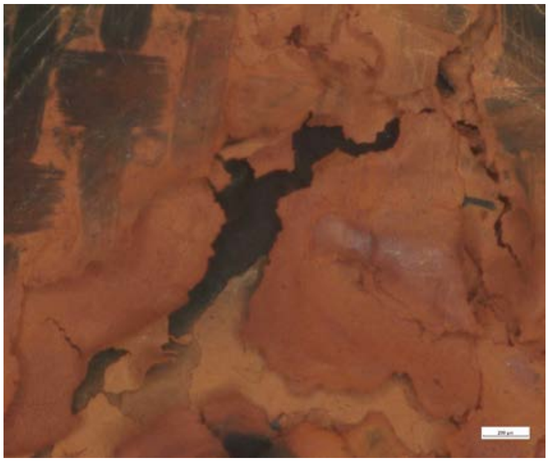

Figure 35. Failure site on sample 2.3. The carbon nanotube surface layer fails suddenly releasing the gas pressure.

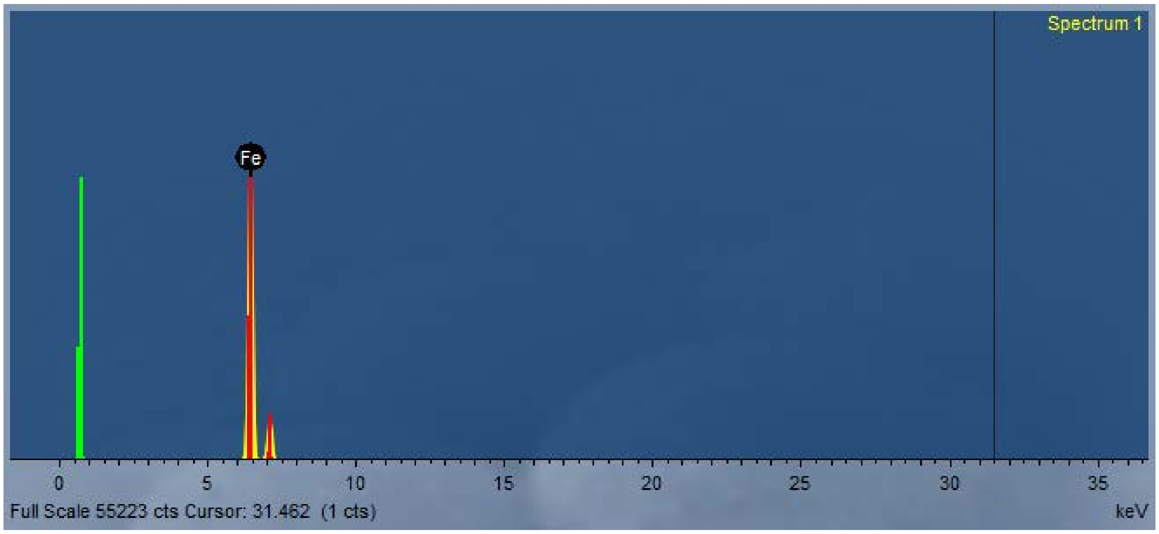

Figure 36. X-ray fluorescence spectrum of the surface of carbon nanotube sample that has been degraded by irradiation.

Pure CNT samples were also tested with the CNTs aligned with the laser spot similarly to the pure carbon fiber samples [0° (2.1), 90° (2.2), and 45° (2.3)]. The formation of the gas bubble is most easily seen in sample 2.2, (20 CNT plys, 90°), which was exposed to 14.17 W and formed the gas bubble at approximately 40 seconds, unlike the 20 plys of 0° (2.1) and 20 plys of 45° (2.3) oriented nanotubes when exposed to 14.17 W which did not form a gas bubble when subjected to the same irradiance. This degradation can be seen Figure 37 and the comparable shots at 2.25W/cm^2, which caused no degradation, for sample 2.1 and 2.3 can be found in the appendix.

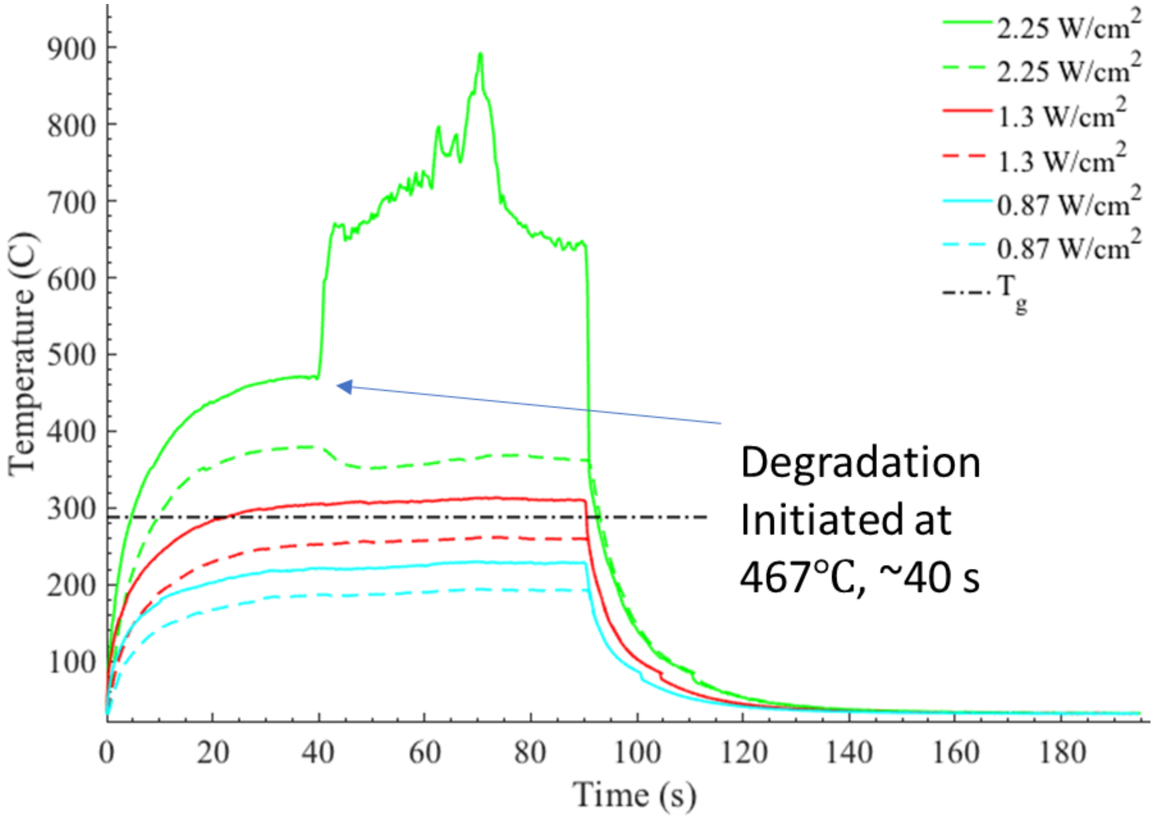

Figure 37. Repeated exposure at increasing laser irradiance of Sample 2.2, exhibiting simple heat diffusion behavior until degradation with average 2.25 W/cm^2. Solid lines are frontside curves, dashed lines are backside curves.

In sample 2.2 (20 CNT plys, 90°), 2.25 W/cm^2produced simple heating and diffusion of heat through the sample for the first 45 seconds. After this point, resin decomposition began and a bubble of these volatile products developed within the laminate that raised the top few layers above the rest. The trapped gases in the bubble structure reduced the contact between layers and decreased the through thickness thermal conductivity significantly. This resulted in a rapid rise in frontside temperature and a reduction in backside steady state temperature. As a result, the backside peak temperature cooled down to this new steady state temperature due to radiation losses and radial conduction. The location of this bubble and the size of this insulating layer can be seen in the spatial distribution graph and the visible damage seen in Figure 38.

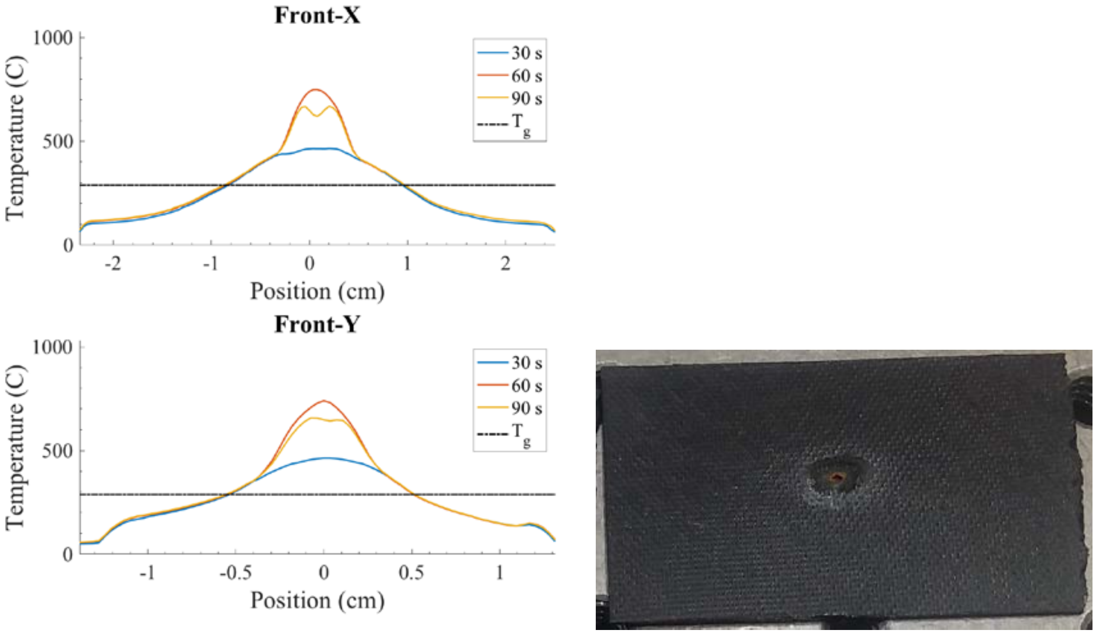

Figure 38. The spatial distribution of the heat (left) and the corresponding damage (right) in Sample 2.2 (20 ply CNTs 90 degree orientation) when exposed to an average irradiance of $2.25\ W/\ cm^2$. (--) 30 secs, (--) 60 secs, (--) 90 secs. The horizontal line is the glass transition temperature of 288 ℃.

Oxidation is a thermally activated process and the increased surface temperature greatly accelerates the oxidation of the CNT layers that form the skin of the bubble. Eventually, as described above, the CNTs can no longer contain the high-pressure decomposition gases. The downside of this reaction is the degradation of the material that supports the reduction of the backside temperatures. This is most easily seen in sample 2.1(20 CNT plys, 0°) and 2.3 (20 CNT plys, 45°), at 6.48 W/cm^2, which both exhibited rapid heating, quick production of organic volatiles, and formation of a protective gas bubble. The thermal response of these samples is shown below in Figure 39 and 40.

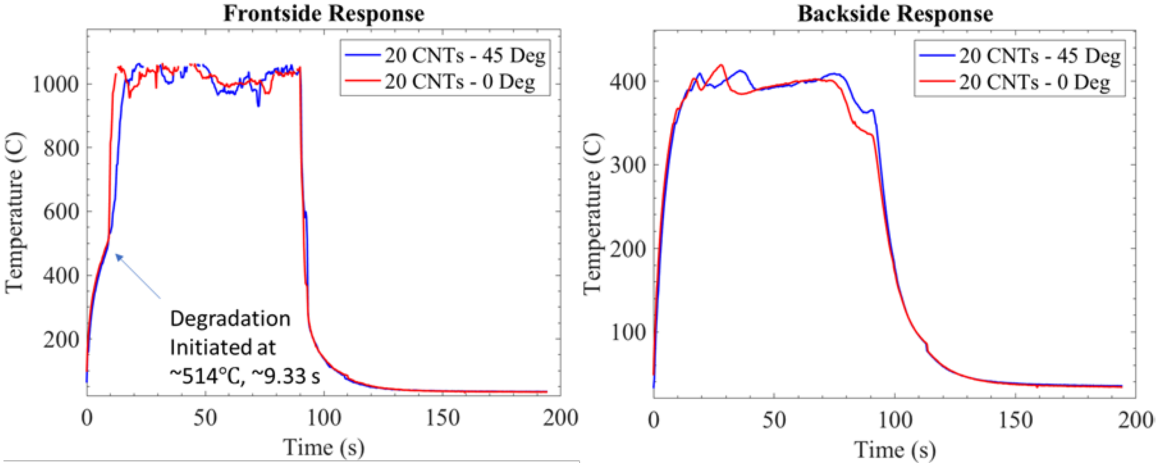

Figure 39. Thermal response of the average hottest pixel when the 0-degree and 45-degree 20 ply CNT samples were exposed to an average irradiance of $4.01\ W/cm^2$.

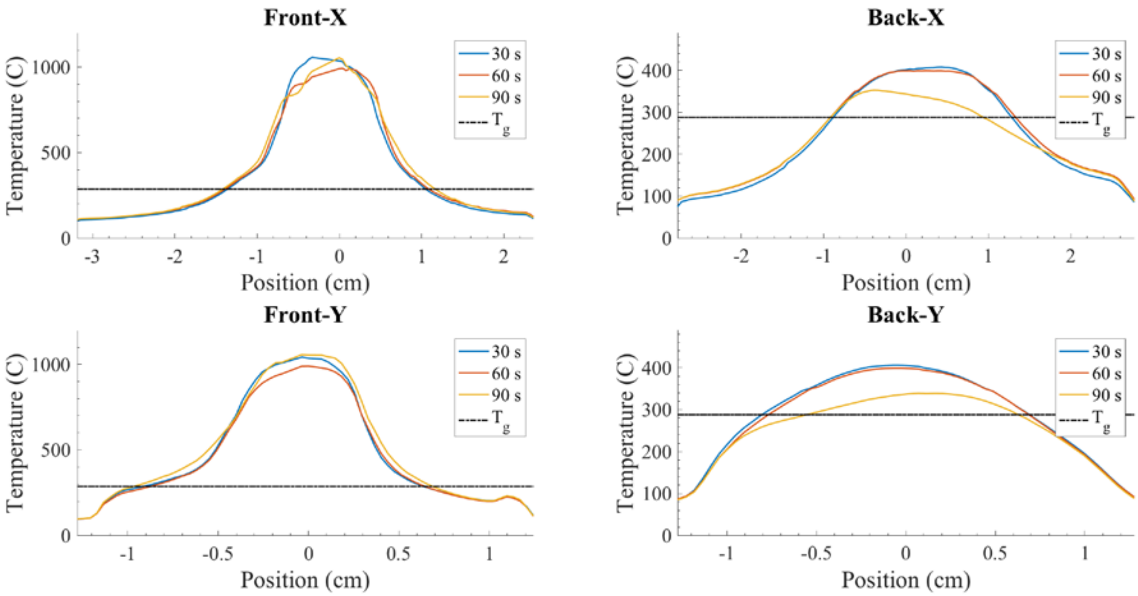

Figure 40. Spatial distribution of heat in sample 2.1 (20 CNT plys, 0°) when exposed to an average irradiance of $4.01\ W/cm^2$. Delamination concentrated heat in the center on the front side and reduced backside steady state temperatures significantly. (--) 30 secs, (--) 60 secs, (--) 90 secs

Degradation for sample 2.2 (20 CNT plys, 90°) initiated around 467 ℃, while for the other carbon nanotube samples it occurred around 514 ℃. The backside steady state temperatures are inconclusive in the tests of sample 2.1 (20 CNT plys, 0°) and 2.3 (20 CNT plys, 45°) because it appears the backside was still cooling down to the newly established steady state temperature. However, it can be seen that sample 2.1 reached a peak temperature around 430 ℃ and cooled down to 350 ℃ before the laser was turned off. In sample 2.3 there was a similar behavior cooling down to 380 ℃ from 425℃. In sample 2.2 (20 CNT plys, 90°) the backside steady state dropped from 380 ℃ to 360 ℃. This is small by comparison to the other two and is likely due to the size of the produced delamination seen in Figure 34. In all cases, heat penetration from laser induced degradation was reduced after degradation had occurred.

Hybrid Laminate Results

The hallmark of composite materials is that they combine the favorable properties of the constituent materials to form a more useful material. The hybrid laminates displayed exactly that behavior by utilizing the benefits of both the carbon fiber and the carbon nanotubes. Despite having less mass, density, thickness, and plies than the carbon fiber samples, the hybrid samples outperformed them with significantly lower backside temperatures in response to the same irradiance. In addition, the hybrid samples with carbon fibers on the surface had lower frontside temperatures than the carbon nanotube samples, however these samples were more massive than the carbon nanotube samples.

To aid understanding of the results, discussion of the hybrid laminates will be broken into three subsections. The first subsection of will consist of the hybrid laminates that had 1-3 CNT layers in the center. Additionally sample 3.1 will also be included on all plots for comparison to the hybrid samples because it contains the same carbon fiber layers that all hybrid samples contain. The CNT content of the hybrid samples will be annotated with a shorthand notation on the graphs. For example, designation (2,1 CNTs) indicates 2 CNT inner layers and 1 CNT outer layer. The sample designations for all samples can be visually seen in Figure 41. and are listed in Table 5 for the first subsection of samples.

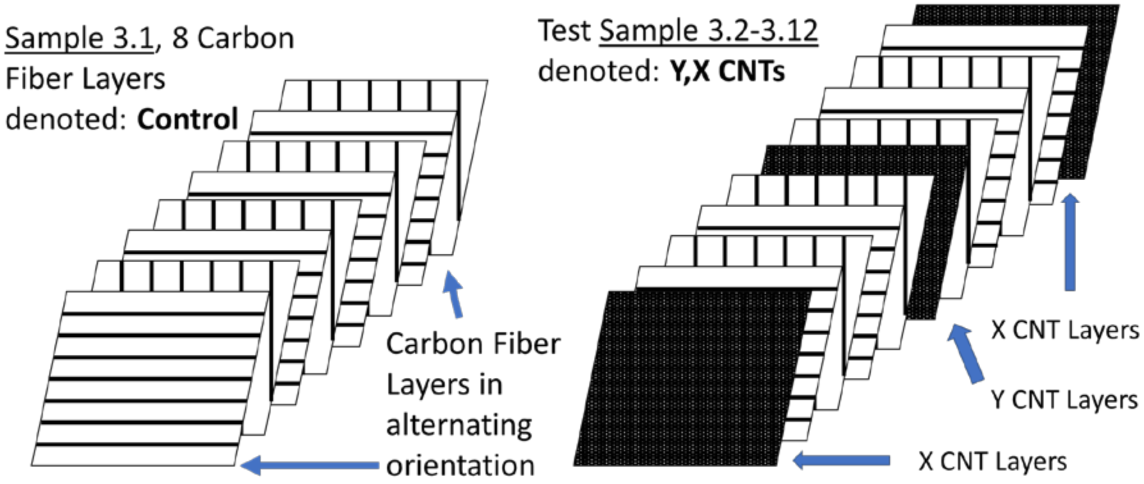

Figure 41. Visual breakdown of the Hybrid Laminate Structure layup. Hybrid Samples are denoted Y,X CNTs indicating Y inner layers and X outer layers.

Table 5. Hybrid Samples with 0-3 CNT center layers

Test #	Orientation
3.1	[0, 90]x4 Stacks
3.2	[0,90,0,90,CNT,90,0,90,0]
3.3	[0,90,0,90,CNT,CNT,90,0,90,0]
3.4	[0,90,0,90,CNT,CNT,CNT,90,0,90,0]

In all of the hybrid laminate samples, the laminates contained eight carbon fiber layers in alternating 0 °, 90 ° directions. For the carbon fiber sample, sample 3.1, this alteration of layers resulted in marginally lower backside temperatures than the 20 ply carbon fiber samples of sample 1.1 and 1.3 despite being only eight plies. The addition of CNT layers further reduced the backside temperature with the help of their good in-plane thermal conductivity and their reduction in through-thickness conductivity caused by the layer of trapped gases. Sample 3.2 showed the lowest average backside temperatures with a minimum at approximately 285 ℃, however sample 3.4 also reached

285 ℃ before laser turn off, so it is hard to tell which sample would have had the lower backside steady state temperature. The individual samples' thermal response can be seen in Figure 42.

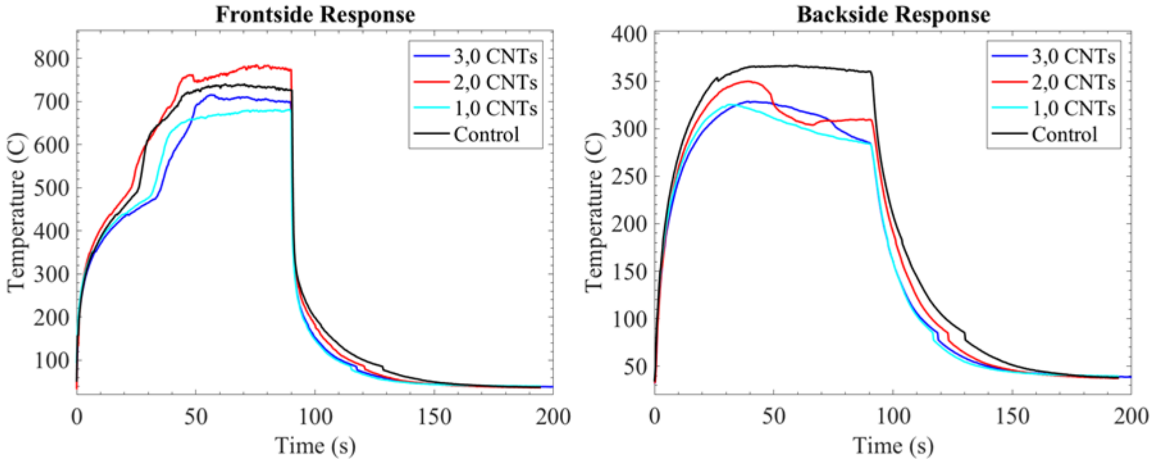

Figure 42. Thermal response of the average hottest pixel when the hybrid samples with 1-3 CNT center layers were exposed to an average irradiance of 6.48 $W/\ cm^2$. The control contained no CNT layers and is annotated in black.

The next subsection of hybrid laminates consists of hybrid laminates that have combinations of CNT layers on the outer edges and the center layers. These samples exhibited similar behavior to the carbon nanotube only samples (2.1-2.3) on the front side with reduced temperatures on the back side. These laminate layups are summarized in Table 6.

Table 6. Hybrid samples with various CNT outer and center layers

Test #	Orientation
3.1	[0, 90]x4 stacks
3.5	[CNT,0,90,0,90,CNT,90,0,90,0,CNT]
3.6	[CNT,0,90,0,90,CNT,CNT,90,0,90,0,CNT]
3.7	[CNT,CNT,0,90,0,90,CNT,90,0,90,0,CNT,CNT]
3.8	[CNT,CNT,0,90,0,90,CNT,CNT,90,0,90,0,CNT,CNT]

These hybrid samples heated up to degradation, followed by bubbling, the bubble bursting, and the restoration of interlayer contact laminate plys. After the destruction of the insulating layer the frontside would cool down to steady state temperatures slightly below sample 3.1 likely due to the extra material available. This whole process translated into an initial cooling on the backside due to delamination of the surfaces and a subsequent increase in temperature when the insulating layer was destroyed. This can be seen in Figure 43. These samples displayed the highest backside temperatures of the hybrid samples despite having more CNTs than the previously discussed samples. This was unexpected because they have more mass and more layers to conduct heat through. This may be due to a larger absorptivity in carbon nanotube surface layers coupling more heat into the material and causing the behavior of the previous samples to be obscured in these samples. In addition, a larger absorptivity, and by extension emissivity, would yield lower true temperature reading when emissivity corrected, so it could be that if these had a higher emissivity, a more correct emissivity correction would actually show a lower temperature than currently shown. Ultimately, the higher absorptivity would be detrimental to thermal protection and it may be more advantageous to put carbon nanotubes in the layers beneath a carbon nanotube surface. The thermal response of these samples is shown in Figure 43.

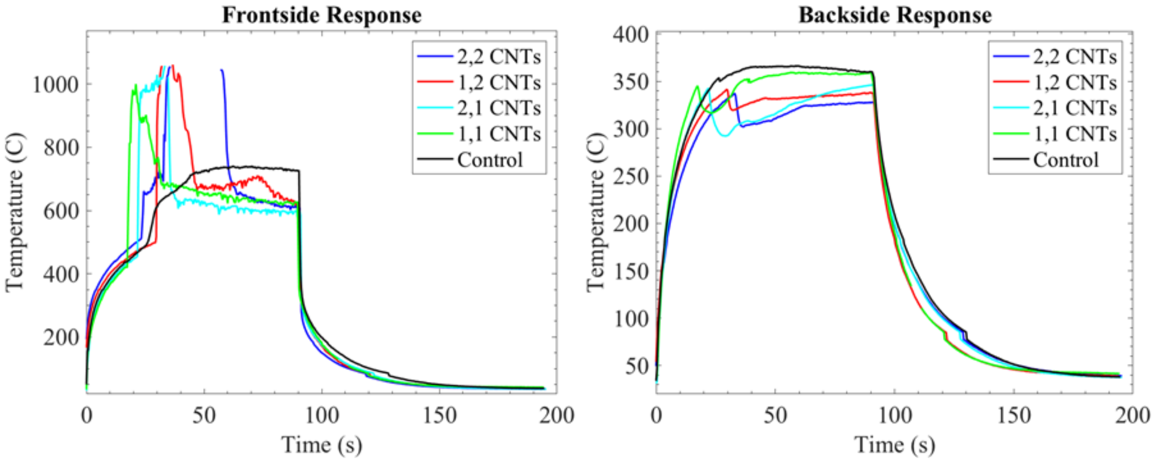

Figure 43. Thermal response of the average hottest pixel when the hybrid samples with 1-2 CNT center and outer layers were exposed to an average irradiance of 6.48 $W/\ cm^2$. The control contained no CNT layers and is annotated in black.

The final subsection of hybrid samples all contained three CNT layers on the edges of the material, with 0-3 CNT layers in the center, all denoted (X,3 CNTs). These samples exhibited the sharpest drop in backside temperature after initial heating and did better or comparably to sample 3.2 (0,1 CNTs) and 3.4 (0,3 CNTs). This sharp drop in backside temperature, which can be seen in Figure 44, was probably due to the rapid formation and duration of the bubbling. The sample that reduced heat penetration to the deeper layers most effectively was sample 3.9 (0,3 CNTs). This is due to the delamination of the top layer reducing heat conduction to the backside. The laminate layups for these samples is annotated in Table 7.

Table 7. Hybrid Samples with 3 CNT Layers on the edges, and 0-3 CNT in the center layer

Test #	Orientation
3.1	[0, 90]x4 stacks
3.9	[CNT,CNT,CNT,0,90,0,90,90,0,90,0,CNT,CNT,CNT]
3.10	[CNT,CNT,CNT,0,90,0,90,CNT,90,0,90,0,CNT,CNT,CNT]
3.11	[CNT,CNT,CNT,0,90,0,90,CNT,CNT,90,0,90,0,CNT,CNT,CNT]
3.12	[CNT,CNT,CNT,0,90,0,90,CNT,CNT,CNT,90,0,90,0,CNT,CNT,CNT]

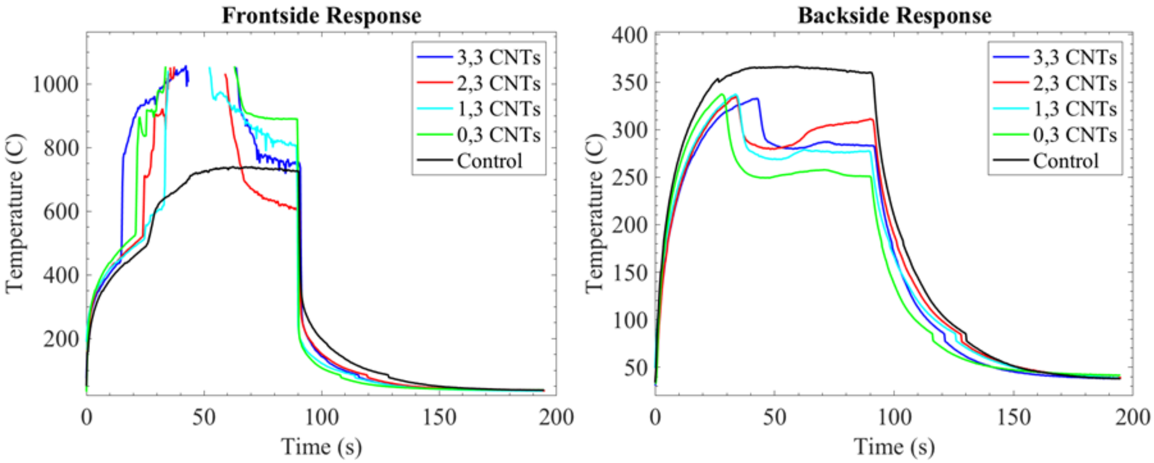

Figure 44. Thermal response of the average hottest pixel when the hybrid samples with three CNT outer layers and 0-3 CNT center layers were exposed to an average irradiance of 6.48 $W/\ cm^2$. The control contained no CNT layers and is annotated in black.

A subset of the thermal response curves, at different irradiances, for sample 3.9 can be seen below in Figure 45. For this sample, backside steady state temperatures approached 270 ℃ under 4.01 W/cm^2 of irradiance. Under 6.68 W/cm^2 of irradiance however, the sample approached 250 ℃. This demonstrated an instance where the backside of a prospective thermal protection layer would experience lower peak temperatures at higher laser powers.

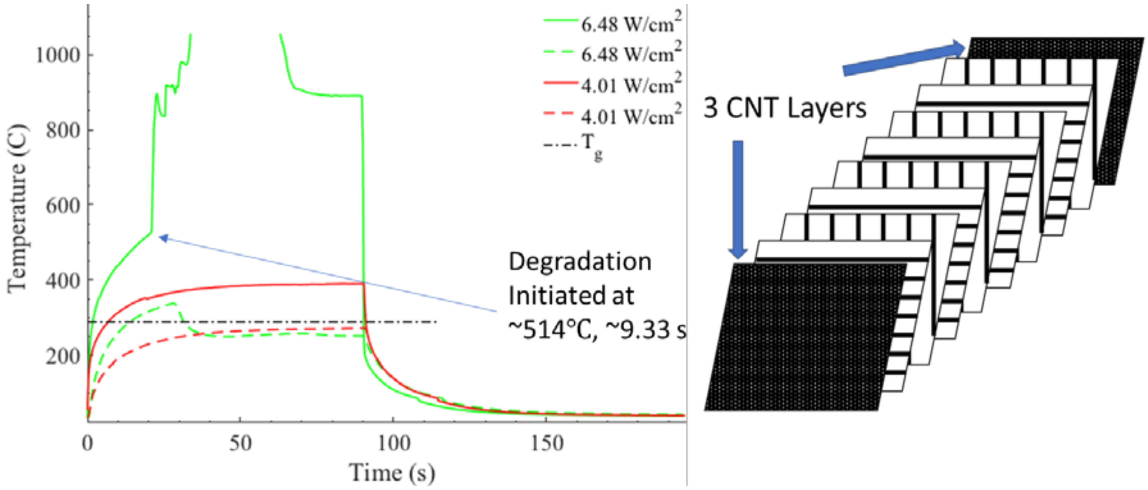

Figure 45. (Left) Thermal response curves for sample 3.9 (0,3 CNTs) at 6.48 and 4.01 W/cm^2. Curves indicate that the heat penetration in a higher irradiance exposure was less than the lower irradiance case. Solid lines are frontside curves, dashed lines are backside curves. (Right) The laminate composition of the sample three CNT outer layers with 8 carbon fiber inner layers.

Summary

Carbon fiber test samples demonstrated how fiber angle can modify the thermal response of a sample subjected to laser irradiation. This effect happens via the effective heat conduction of the thermal load to a larger sample volume. This is not a viable design parameter for thermal protection layers because fiber angle is determined by load constraints. However, this does demonstrate how improved heat conduction via thermal conductivity can improve the thermal resistance of a composite material. This has been noted in various studies incorporating CNTs in composite material [7-10]. This effect was not seen to a large degree in the CNT and hybrid composite samples, due to a different mechanism that occurred. In samples incorporating CNTs, interlaminar gas pressure built up due to the production of organic volatiles in the samples. Due to the gas pressure, the layers delaminated reducing through thickness thermal conductivity. This thermally isolates the deeper layers effectively shielding them from the thermal degradation induced via laser heating. The cost is the rapid heating of the top layers, which accelerates degradation. The sample that reduced heat penetration the most was sample 3.9 (3,0 CNTs), which exhibited rapid cooling to 250 ℃ on the backside when exposed to 6.68 W/cm^2. This was lower than the case when sample 3.9 was exposed to 4.01 W/cm^2, in which backside temperatures approached 270 ℃. The sample that experienced the best reduction in heat penetration relative to the addition of CNT layers was Sample 3.2 (1,0 CNTs). The introduction of one CNT layer in the center reduced heat by 85 ℃ when compared to the control sample.

V. Conclusions

Chapter Overview

The purpose of this chapter is to outline the answers to the investigative questions proposed in chapter 1, discuss the significance of the research, and make recommendations for future work.

Investigative Questions

Table 1 is repeated here for the convenience of the reader.

Table 1. Summary of Research Objectives and Methodology

Research Objectives	Methodology
O1: Characterize Carbon Fiber Thermal Response	Expose samples to various irradiances and record thermal response
O2: Characterize Carbon Nanotube Thermal Response	Expose samples to various irradiances and record thermal response
O3: Characterize Hybrid Samples Thermal Response	Expose samples to various irradiances and record thermal response

Q1: Characterize Carbon Fiber Thermal Response

The cyanate ester carbon fiber composites degraded at temperatures between 480 °C and 520 °C. Fiber angle greatly affected the conduction of heat in the 20 ply carbon fiber samples. A fiber angle of 45° showed a drastic improvement in the distribution of the heat load and subsequently protected sample 1.5 extremely well. Unfortunately, this protection mechanism is not generalizable to other engagements because the response of a particular composite geometry depends on the asymmetry of the beam. Additionally, the edges were not approximately at infinity which would likely be the case in larger structures. Structures with edges at infinity would experience lower peak temperatures and subsequently less degradation because the heat is not trapped at the center. In these cases, the effect of fiber angle on heat conduction will become increasingly small because the effective area of heat conduction due to fiber angle variation will be mitigated provided the number of fibers absorbing the radiation remains. This was the case for the 90° and 45° oriented carbon fiber samples. This would not be the case for carbon fiber samples in the 0° orientation, since the number of fibers absorbing the radiation is significantly reduced by the fiber angle. To the extent that fiber angle orientation affects the number of fibers absorbing the radiation, the variation of fiber angle could have large scale behavior similar to, but to a lesser extent, than the small-scale results shown in this work.

Although fiber angle is not a viable design parameter for thermal protection layers, this did display how thermal conductivity can improve the distribution of the heat load and protect the sample. This was supported by the tests of sample 3.1 which was composed of eight alternating carbon fiber plys. These tests showed lower backside temperatures than the thicker 20-ply carbon fiber samples. This was due to the alternating fiber directions in each layer, which carried heat away in both x and y directions.   This resulted in a more even distribution of heat that allowed the thinner sample to exhibit marginally lower peak backside temperatures when exposed to the same irradiance.

Q2: Characterize the carbon nanotube thermal response

The cyanate ester carbon nanotube laminates degraded at similar temperature thresholds to the carbon fiber composites, but they reached the decomposition temperature sooner due to their lower density, mass, and thickness. When the resin decomposed, the carbon nanotube samples exhibited the formation of a gas pocket behind the CNT layer(s) that acted like a reactive armor that activated and thermally cut-off the top layers, sacrificing them and protecting the layers underneath. This insulating layer reduced heat flow to the backside and caused a reduction in steady state backside temperatures. This comes at the cost of the top layers which heat up rapidly when forced to take more of the heat load and oxidize more rapidly.

Q3: Characterize the hybrid laminate thermal response

The surface layers of the hybrid laminate responded as the corresponding layers in the previous composites responded. If the top layer was carbon fiber it degraded similarly and reached steady state temperatures on the frontside similar to the control sample. If the surface layers were carbon nanotubes they degraded at similar temperatures, but reached them faster than the control and suffered more visible surface damage. This damage was due to similar bubbling that occurred in the carbon nanotubes which reduced the backside temperatures significantly in some hybrid samples.

The hybrids managed to achieve more favorable properties by utilizing the advantages of both materials. At 6.68 W/cm^2, the introduction of one CNT layer at the center dropped backside temperatures from 380 ℃ observed in sample 3.1 (no CNTs), to 285 ℃ in sample 3.2 (1,0 CNTs). This was further improved upon with other samples, most notably sample 3.9 (0,3 CNTs), which showed an even faster cooling of the backside surface and an eventual steady state of 250 ℃. Additionally, the backside steady state temperatures in the 6.68 W/cm^2 test of sample 3.9 (3,0 CNTs) reached lower temperatures than the lower power test at 20.25 W, which meant that the backside layer and prospective layers below this thermal protection layer would have experienced less heating from a higher irradiance.

Significance of Research.

Based on previous research, the introduction of CNTs was expected to improve the thermal resistance of the composite through an increase of the in-plane thermal conductivity of the material [7-10]. This was not largely demonstrated in this work. This research showed that the introduction of CNT layers can improve the thermal resistance of composite materials by trapping the organic volatiles that are produced during decomposition. This is incredibly advantageous in the context of laser hardening because the heat shielding only initiates when laser irradiation is sufficient to induce decomposition. This sacrifices the surface thermal protection layers for the benefit of the deeper layers. With the introduction of one CNT layer in the center, composite backside temperatures were reduced by 85 ℃; a reduction that is significant enough to prevent random scission and cross linking of the hydrocarbon backbone and triazine ring breakdown in material that would have otherwise exceeded 450℃. With optimization , this reactive mechanism could provide laser hardening to composite materials preventing degradation and retaining strength. One added layer increases the composite thickness by 70 μm and mass by 94.5 g/m^2 of material used providing significant thermal protection for volumetric and mass increases comparable to a coat of paint (69.8 g/m^2). Alternatively, this research also suggests that designing thermal protection layers that have very high in-plane thermal conductivities and very low through thickness conductivities could be an effective strategy to prevent heat penetration to deeper layers.

Recommendations for Future Research

Future work should conduct experiments on different arrangements of carbon fiber and carbon nanotube layers to determine more optimal configurations of the materials. The results of this work have shown that a few carbon nanotube layers near the surface of a composite would provide a protective effect via a reduction in through thickness thermal conductivity but these layers suffer increased degradation due to the subsequently higher temperatures. It may be advantageous to put the carbon nanotube layers underneath a couple carbon fiber layers to provide reinforcement and ablative protection to the carbon nanotube layer. This would allow the carbon nanotubes to trap the gas, creating the protective effect, while simultaneously suffering less oxidation and degradation. Future experiments should place 1-5 carbon nanotube layers at varying depths in a carbon fiber composite material to investigate how to maximize the reduction in heat penetration and protection of the carbon fibers. The optimal depth will likely be near the surface where temperatures, and subsequently organic volatile production, are the highest.

Future work should also conduct experiments on thermal protection layers that alternate materials with high in plane thermal conductivity and low through thickness thermal conductivity. Materials with this make up would cause a majority of the heat load to be at the surface and would subsequently reduce heat penetration. A great insulating material for this would be aero-gel and aero-gel like materials. Their insulative properties could prevent heat penetration and preserve the composite strength of the deeper layers.

In addition to more laser degradation testing, strength testing should be performed on similarly degraded samples to ensure that the reduction in heat penetration resulted in a larger preservation of strength. This could be done on the samples with carbon nanotubes at various depths in the composite to find the optimal arrangement for strength preservation in in situ engagement scenarios.

Appendix

The appendix contains the family of curves for each of the samples exposed to various irradiances. These graphs are the thermal response of the hottest pixel in the scene.

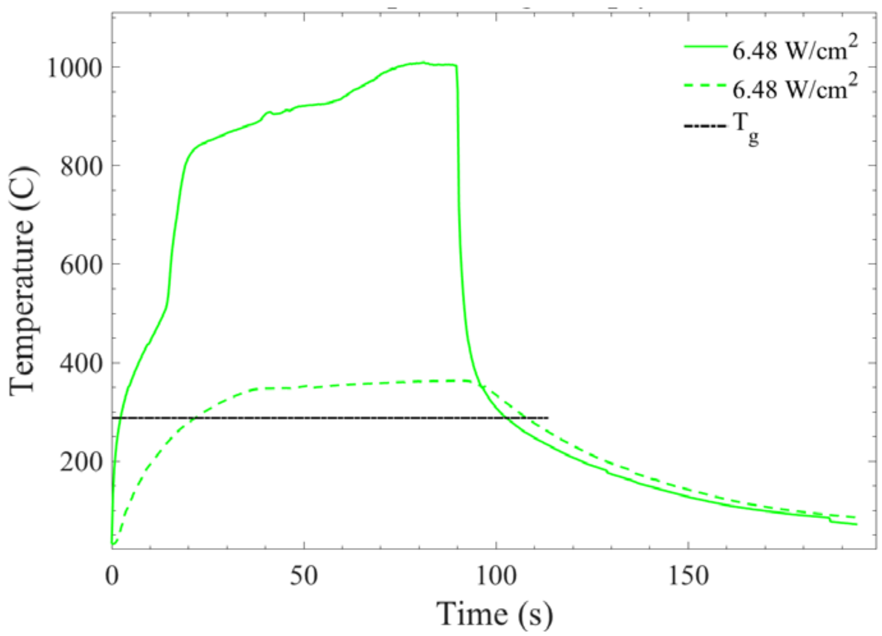

Figure A. 1 Thermal response of Sample 1.1 (20 plys CF, 0-degree orientation) exposed to 6.68 W/cm^2 of irradiance. Solid lines are frontside curves, dashed lines are backside curves.

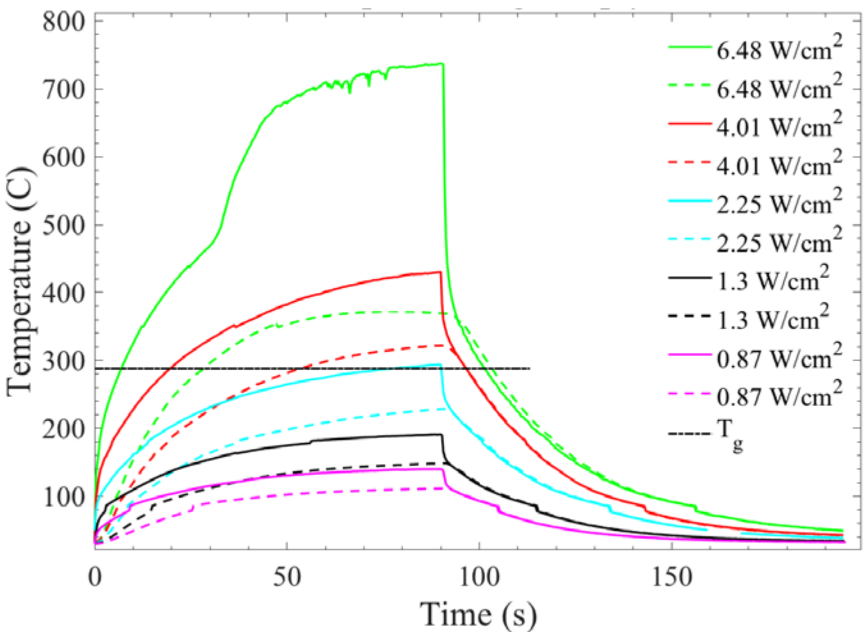

Figure A. 2 Thermal response of Sample 1.3 (20 plys CF, 90-degree orientation) repeatedly exposed to various irradiances. Solid lines are frontside curves, dashed lines are backside curves.

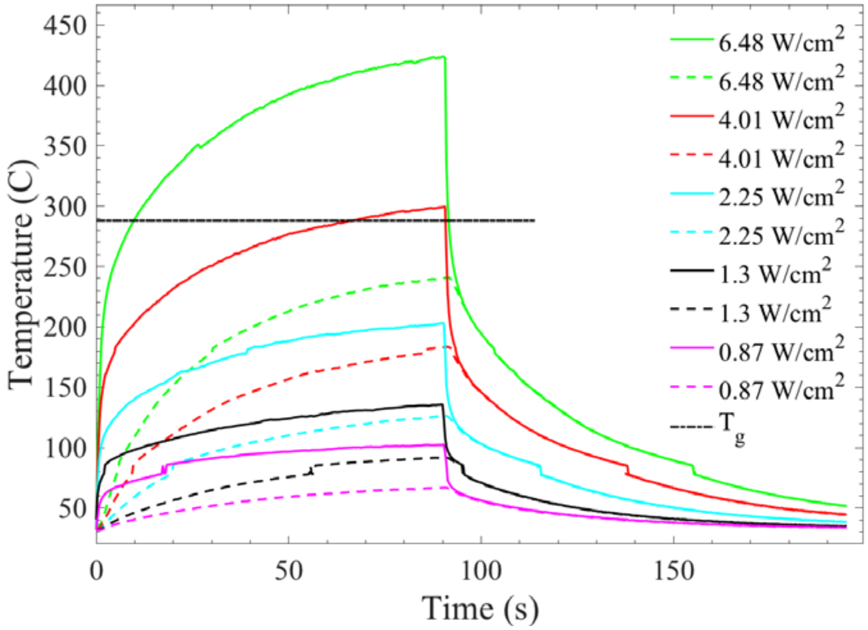

Figure A. 3 Thermal response of Sample 1.5 (20 plys CF, 45-degree orientation) repeatedly exposed to various irradiances. Solid lines are frontside curves, dashed lines are backside curves.

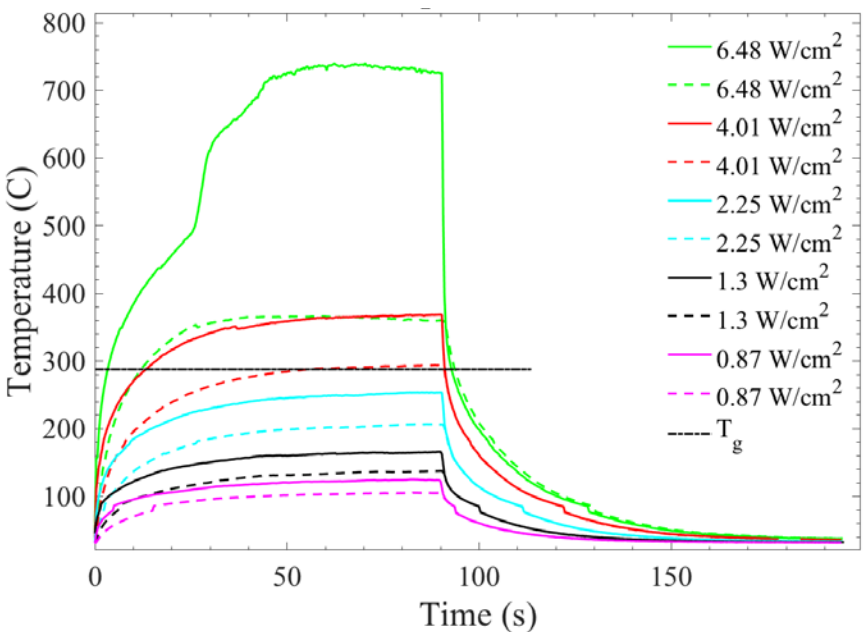

Figure A. 4 Thermal response of Sample 3.1 (0 CNT Center Layers, 0 CNT Outer Layers) repeatedly exposed to various irradiances. Solid lines are frontside curves, dashed lines are backside curves.

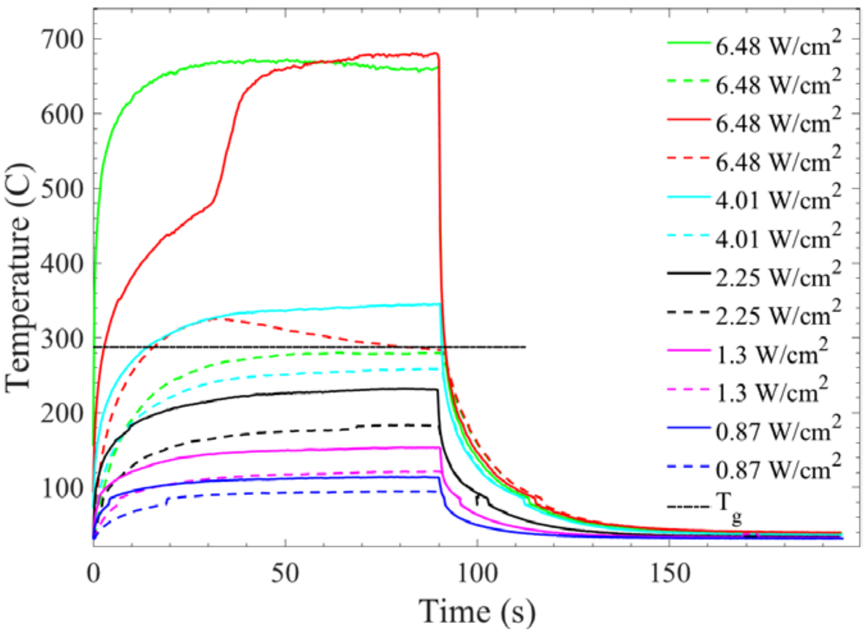

Figure A. 5 Thermal response of Sample 3.2 (1 CNT Center Layers, 0 CNT Outer Layers) repeatedly exposed to various irradiances. Solid lines are frontside curves, dashed lines are backside curves.

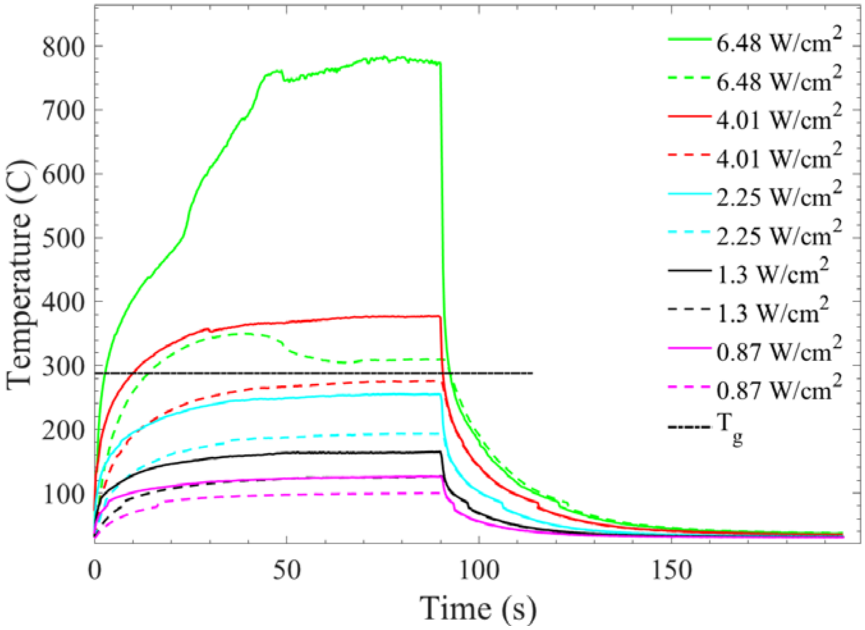

Figure A. 6 Thermal response of Sample 3.3 (2 CNT Center Layers, 0 CNT Outer Layers) repeatedly exposed to various irradiances. Solid lines are frontside curves, dashed lines are backside curves.

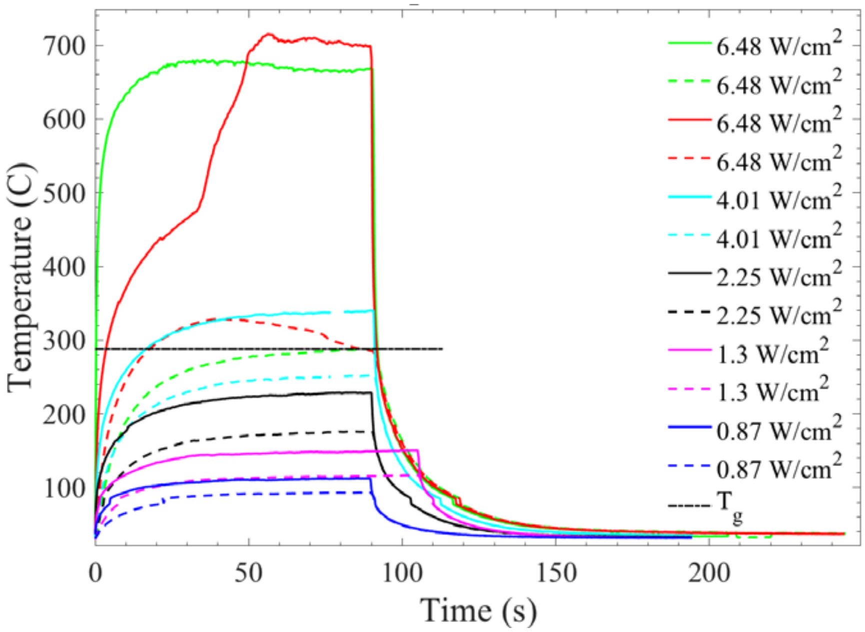

Figure A. 7 Thermal response of Sample 3.4 (3 CNT Center Layers, 0 CNT Outer Layers) repeatedly exposed to various irradiances. Solid lines are frontside curves, dashed lines are backside curves.

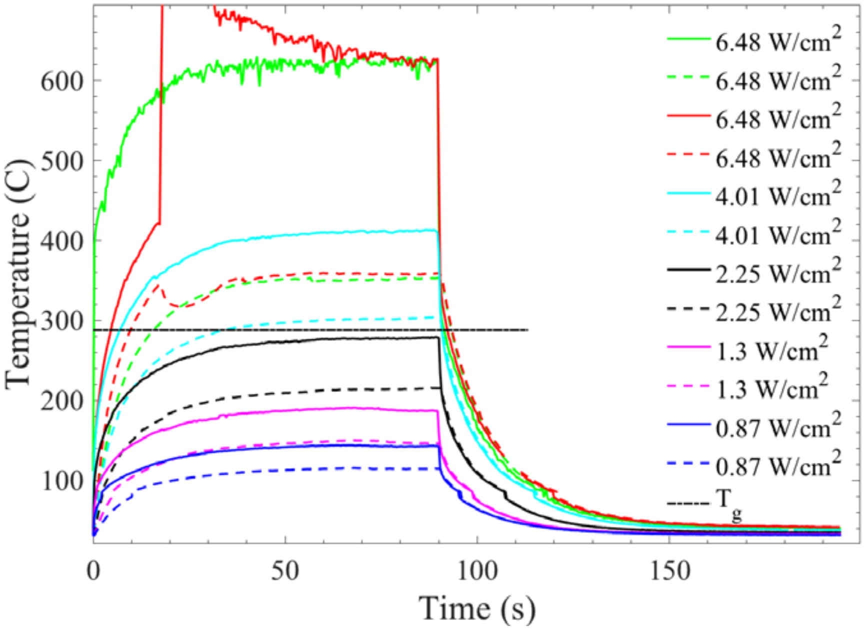

Figure A. 8 Thermal response of Sample 3.5 (1 CNT Center Layers, 1 CNT Outer Layers) repeatedly exposed to various irradiances. Solid lines are frontside curves, dashed lines are backside curves.

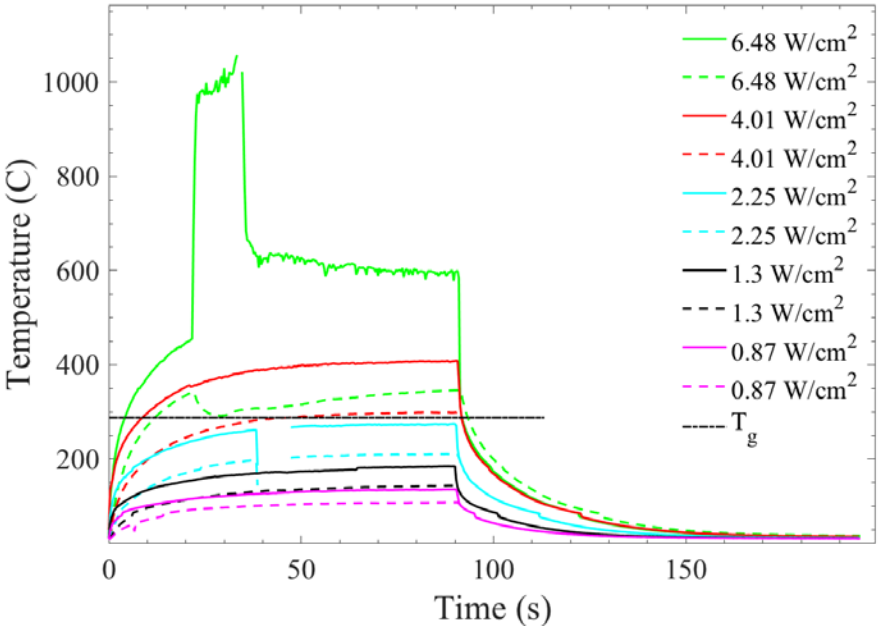

Figure A. 9 Thermal response of Sample 3.6 (2 CNT Center Layers, 1 CNT Outer Layers) repeatedly exposed to various irradiances. Solid lines are frontside curves, dashed lines are backside curves.

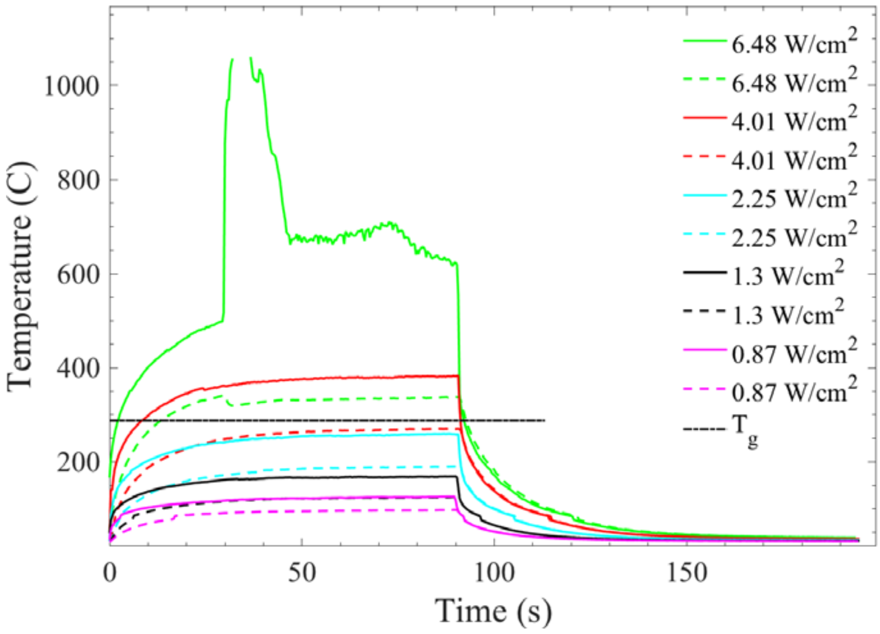

Figure A. 10 Thermal response of Sample 3.7 (1 CNT Center Layers, 2 CNT Outer Layers) repeatedly exposed to various irradiances. Solid lines are frontside curves, dashed lines are backside curves

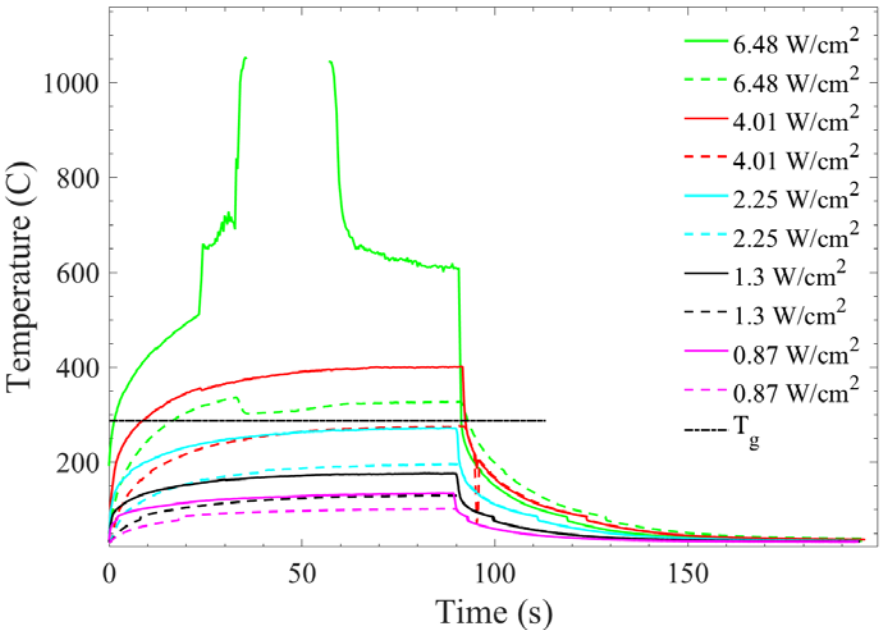

Figure A. 11 Thermal response of Sample 3.8 (2 CNT Center Layers, 2 CNT Outer Layers) repeatedly exposed to various irradiances. Solid lines are frontside curves, dashed lines are backside curves.

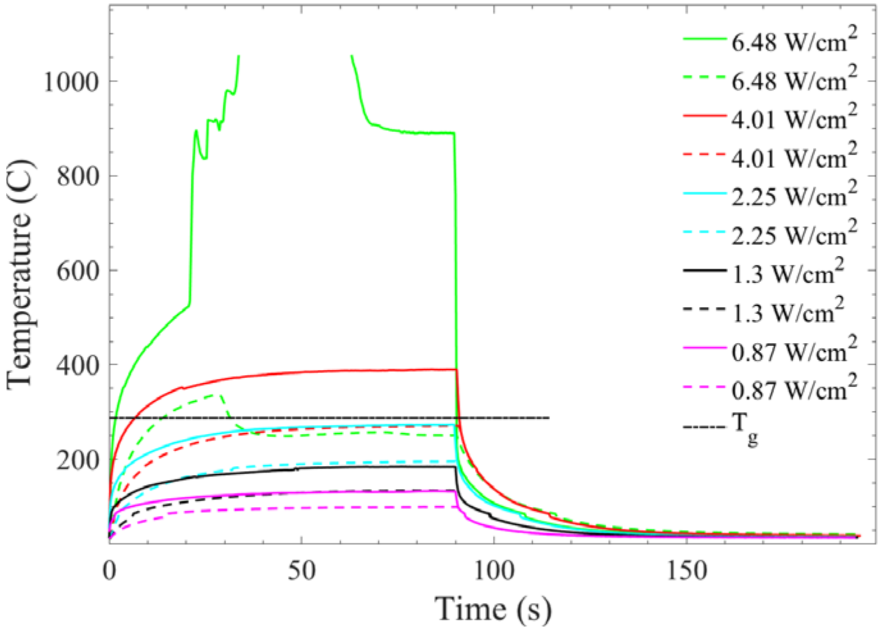

Figure A. 12 Thermal response of Sample 3.9 (0 CNT Center Layers, 3 CNT Outer Layers) repeatedly exposed to various irradiances. Solid lines are frontside curves, dashed lines are backside curves.

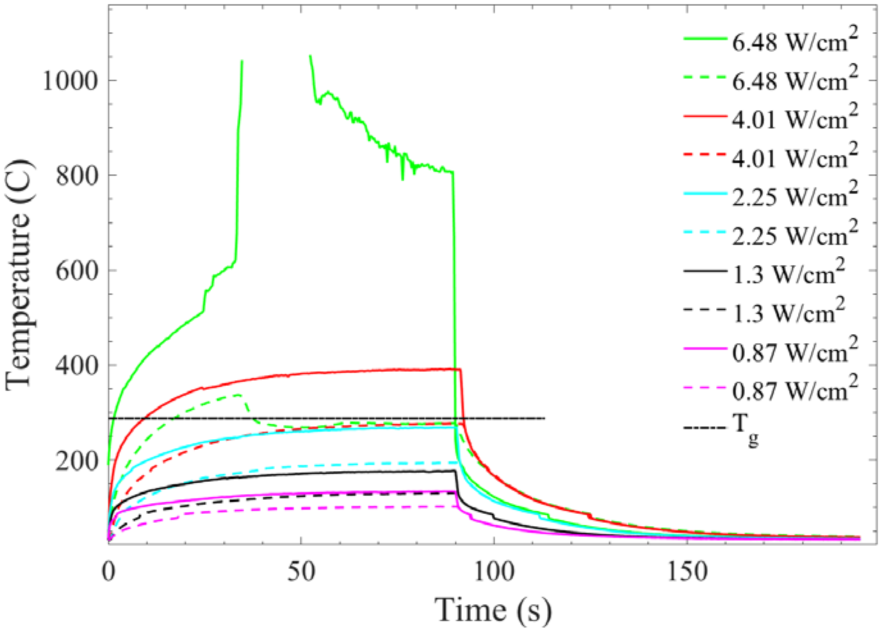

Figure A. 13 Thermal response of Sample 3.10 (1 CNT Center Layers, 3 CNT Outer Layers) repeatedly exposed to various irradiances. Solid lines are frontside curves, dashed lines are backside curves.

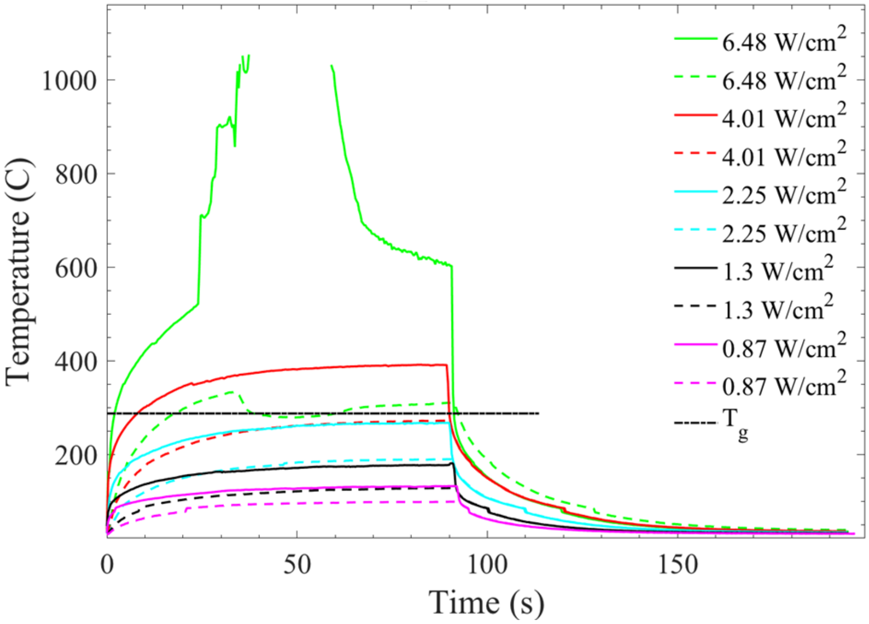

Figure A. 14 Thermal response of Sample 3.11 (2 CNT Center Layers, 3 CNT Outer Layers) repeatedly exposed to various irradiances. Solid lines are frontside curves, dashed lines are backside curves.

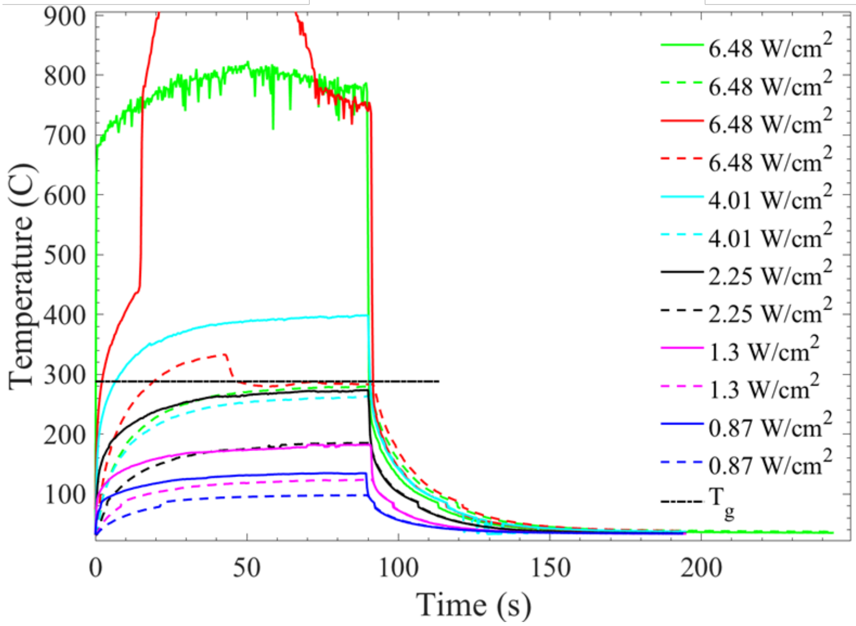

Figure A. 15 Thermal response of Sample 3.12 (3 CNT Center Layers, 3 CNT Outer Layers) repeatedly exposed to various irradiances. Solid lines are frontside curves, dashed lines are backside curves.

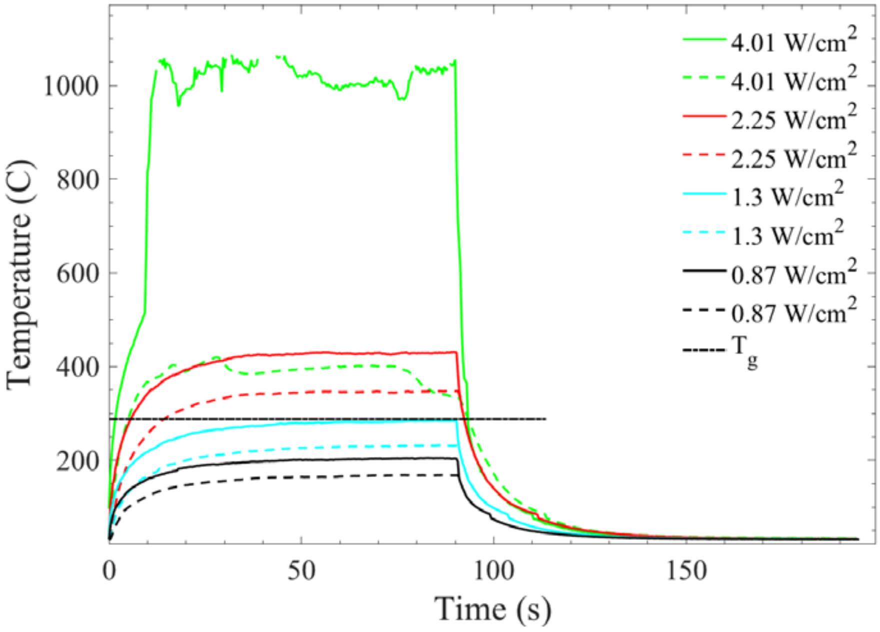

Figure A. 16 Thermal response of Sample 2.1 (20 CNT plys, 0-degree orientation) repeatedly exposed to various irradiances. Solid lines are frontside curves, dashed lines are backside curves.

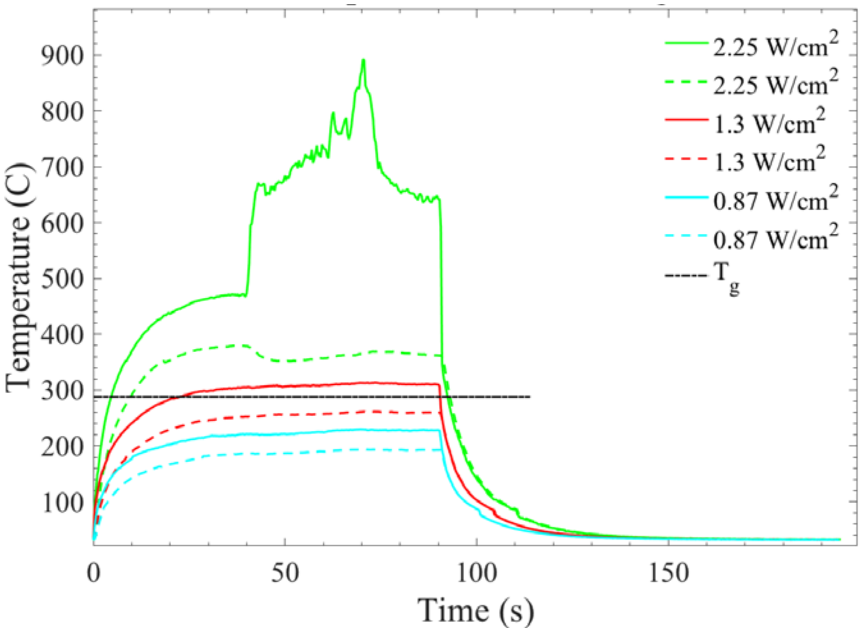

Figure A. 17 Thermal response of Sample 2.2 (20 CNT plys, 90-degree orientation) repeatedly exposed to various irradiances. Solid lines are frontside curves, dashed lines are backside curves.

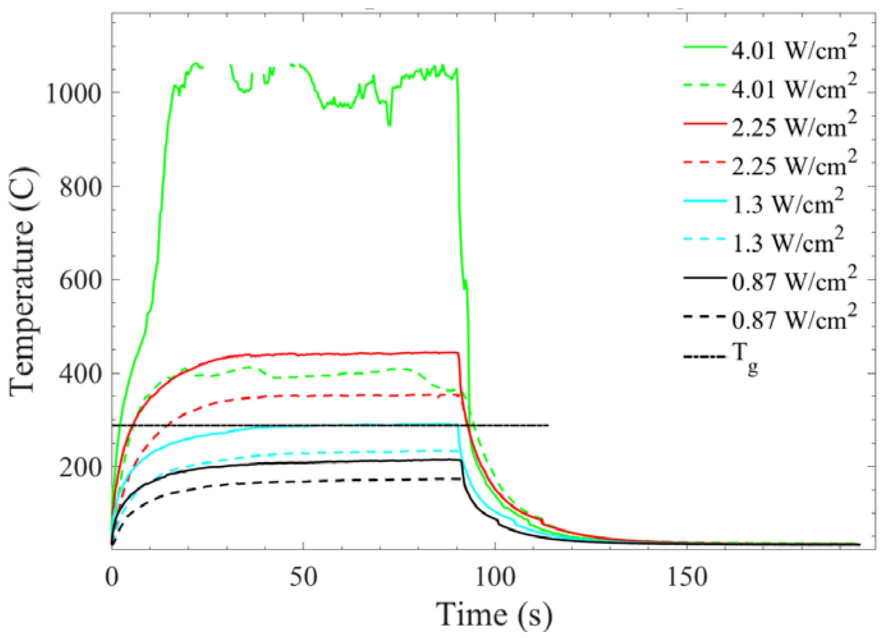

Figure A. 18 Thermal response of Sample 2.3 (20 CNT plys, 45-degree orientation) repeatedly exposed to various irradiances. Solid lines are frontside curves, dashed lines are backside curves.

Bibliography

1. Einstein, A. (1972). On the quantum theory of radiation [in] Laser Theory, ed. FA Barnes.
2. Hecht, J. (2010). A short history of laser development. *Applied optics*, *49*(25), F99-F122.
3. Sprangle, P., Ting, A., Penano, J., Fischer, R., & Hafizi, B. (2008). *Incoherent combining of high-power fiber lasers for directed-energy applications* (No. NRL/MR/6790-08-9096). NAVAL RESEARCH LAB WASHINGTON DC BEAM PHYSICS BRANCH.
4. Soutis, C. (2005). Fibre reinforced composites in aircraft construction. *Progress in Aerospace Sciences*, *41*(2), 143-151.
5. Herr, N. C., Gonzales, A. E., & Perram, G. P. (2018). Kinetics, evolving thermal properties, and surface ignition of carbon fiber reinforced epoxy composite during laser-induced decomposition. *Polymer degradation and stability*, *152*, 147-161.
6. Herr, N. C. (2016). *Degradation of carbon fiber reinforced polymer and graphite by laser heating* (No. AFIT-ENP-DS-16-S-025). Air Force Institute of Technology WPAFB.
7. Park, J. M., Kwon, D. J., Wang, Z. J., Roh, J. U., Lee, W. I., Park, J. K., & DeVries, K. L. (2014). Effects of carbon nanotubes and carbon fiber reinforcements on thermal conductivity and ablation properties of carbon/phenolic composites. *Composites Part B: Engineering*, *67*, 22-29.
8. Wang, Z. J., Kwon, D. J., Gu, G. Y., Lee, W. I., Park, J. K., DeVries, K. L., & Park, J. M. (2014). Ablative and mechanical evaluation of CNT/phenolic composites by thermal and microstructural analyses. *Composites Part B: Engineering*, *60*, 597-602.
9. Wu, Q., Zhu, W., Zhang, C., Liang, Z., & Wang, B. (2010). Study of fire retardant behavior of carbon nanotube membranes and carbon nanofiber paper in carbon fiber reinforced epoxy composites. *Carbon*, *48*(6), 1799-1806
10. Liu, Z., Hao, A., Zhang, S., Dessureault, Y. S., & Liang, R. (2019). Lightweight carbon nanotube surface thermal shielding for carbon fiber/bismaleimide composites. *Carbon*, *153*, 320-329.
11. O'connell, M. J. (2006). *Carbon nanotubes: properties and applications*. CRC press
12. Iijima, S. (1991). Helical microtubules of graphitic carbon. *nature*, *354*(6348), 56.
13. Ali, M. E., Das, R., Maamor, A., & Hamid, S. B. A. (2014). Multifunctional carbon nanotubes (CNTs): a new dimension in environmental remediation. In *Advanced Materials Research* (Vol. 832, pp. 328-332). Trans Tech Publications.
14. Zhao, Y. L., & Stoddart, J. F. (2009). Noncovalent functionalization of single-walled carbon nanotubes. *Accounts of chemical research*, *42*(8), 1161-1171.
15. O'Keefe, J. C. (2019). *Mechanical and Vibration Characterization of Hybrid Carbon Nanotube Laminates* (No. AFIT/GMS/ENY/19-M-310). AIR FORCE

INST OF TECH WRIGHT-PATTERSON AFB OH SCHOOL OF ENGINEERING AND MANAGEMENT.

16. Jorio, A., Dresselhaus, G., & Dresselhaus, M. S. (Eds.). (2007). *Carbon nanotubes: advanced topics in the synthesis, structure, properties and applications* (Vol. 111). Springer Science & Business Media.
17. Che, J., Cagin, T., & Goddard III, W. A. (2000). Thermal conductivity of carbon nanotubes. *Nanotechnology*, *11*(2), 65.
18. Kessler, Michael. (2012). Cyanate Ester Resins Adapted from Cyanate Ester Resins, First Edition… 10.1002/9781118097298.weoc062.
19. Lyon, R. E., Walters, R., & Gandhi, S. (2002). *Combustibility of cyanate ester resins* (No. DOT/FAA/AR-02/44). WILLIAM J HUGHES TECHNICAL CENTER ATLANTIC CITY NJ.
20. Ramirez, M. L., Walters, R., Lyon, R. E., & Savitski, E. P. (2002). Thermal decomposition of cyanate ester resins. *Polymer degradation and stability*, *78*(1), 73-82.
21. Chung, K., & Seferis, J. C. (2001). Evaluation of thermal degradation on carbon fiber/cyanate ester composites. *Polymer degradation and stability*, *71*(3), 425-434.
22. Park, S. J., & Heo, G. Y. (2015). Precursors and manufacturing of carbon fibers. In *Carbon Fibers* (pp. 31-66). Springer, Dordrecht.
23. Khayyam, H., Jazar, R. N., Nunna, S., Golkarnarenji, G., Badii, K., Fakhrhoseini, S. M., ... & Naebe, M. (2019). PAN Precursor Fabrication, Applications and Thermal Stabilization Process in Carbon Fiber Production: Experimental and Mathematical Modelling. *Progress in Materials Science*, 100575.
24. Liu, Y., & Kumar, S. (2012). Recent progress in fabrication, structure, and properties of carbon fibers. *Polymer Reviews*, *52*(3), 234-258
25. Sayed, U. A., Shirsat, A., Shinde, A., & Lahariya, A. (2015). Manufacturing of Acrylic Fibres with Desirable Properties to Make Carbon Fibres-Review
26. Pradère, C., Batsale, J. C., Goyhénèche, J. M., Pailler, R., & Dilhaire, S. (2009). Thermal properties of carbon fibers at very high temperature. *Carbon*, *47*(3), 737-743.
27. Baddour, Carole E., and Cedric Briens. "Carbon nanotube synthesis: a review." *International journal of chemical reactor engineering* 3.1 (2005).
28. Wu, Y., Zhang, X., Leung, A. Y. T., & Zhong, W. (2006). An energy-equivalent model on studying the mechanical properties of single-walled carbon nanotubes. *Thin-walled structures*, *44*(6), 667-676.
29. Grady BP. Carbon nanotube composites. University of Oklahoma. Available from: <http://coecs.ou.edu/Brian.P.Grady/nanotube.html>
30. Rafiee, R., & Pourazizi, R. (2014). Evaluating the influence of defects on the young's modulus of carbon nanotubes using stochastic modeling. *Materials Research*, *17*(3), 758-766.
31. Aliev, A. E., Lima, M. H., Silverman, E. M., & Baughman, R. H. (2009). Thermal conductivity of multi-walled carbon nanotube sheets: radiation losses and quenching of phonon modes. *Nanotechnology*, *21*(3), 035709.

32. Boley, C. D., & Rubenchik, A. M. (2013). Modeling of laser interactions with composite materials. *Applied optics*, *52*(14), 3329-3337.
33. Mizuno, K., Ishii, J., Kishida, H., Hayamizu, Y., Yasuda, S., Futaba, D. N., ... & Hata, K. (2009). A black body absorber from vertically aligned single-walled carbon nanotubes. *Proceedings of the National Academy of Sciences*, *106*(15), 6044-6047.
34. Mouritz, A. P., & Gibson, A. G. (2007). *Fire properties of polymer composite materials* (Vol. 143). Springer Science & Business Media.
35. Feih, S., & Mouritz, A. P. (2012). Tensile properties of carbon fibres and carbon fibre–polymer composites in fire. *Composites Part A: Applied Science and Manufacturing*, *43*(5), 765-772.
36. Al-Mayman, S. I., Al-Abbadi, N. M., & Atieh, M. A. (2014). Thermal oxidation kinetic of carbon nanotubes (CNTs). Arabian Journal for Science and Engineering, 39(2), 621-630.
37. Boyd, R. W. (1983). Radiometry and the detection of optical radiation.
38. Shell, J. R. (2004). Bidirectional reflectance: An overview with remote sensing applications & measurement recommendations. *Rochester NY*.
39. Nicodemus, F. E., Richmond, J. C., Hsia, J. J., Ginsberg, I. W., & Limperis, T. (1992). Geometrical considerations and nomenclature for reflectance. *NBS monograph*, *160*, 4.

REPORT DOCUMENTATION PAGE	*Form Approved* *OMB No. 074-0188*

1. REPORT DATE *(DD-MM-YYYY)* 26-03-2020	**2. REPORT TYPE** Master’s Thesis	**3. DATES COVERED** *(From – To)* May 2018 – May 2020

TITLE AND SUBTITLE Laser Induced Thermal Degradation of Carbon Fiber-Carbon Nanotube Hybrid Laminates	**5a. CONTRACT NUMBER**
	5b. GRANT NUMBER
	5c. PROGRAM ELEMENT NUMBER
6. AUTHOR(S) Key, Joshua A., 1st Lieutenant, USAF	**5d. PROJECT NUMBER**
	5e. TASK NUMBER
	5f. WORK UNIT NUMBER

7. PERFORMING ORGANIZATION NAMES(S) AND ADDRESS(S)

Air Force Institute of Technology
Graduate School of Engineering and Management (AFIT/ENY)
2950 Hobson Way, Building 640
WPAFB OH 45433-8865

8. PERFORMING ORGANIZATION REPORT NUMBER

AFIT-ENP-MS-20-M-104

9. SPONSORING/MONITORING AGENCY NAME(S) AND ADDRESS(ES)

Intentionally Left Blank

10. SPONSOR/MONITOR’S ACRONYM(S)

11. SPONSOR/MONITOR’S REPORT NUMBER(S)

12. DISTRIBUTION/AVAILABILITY STATEMENT

DISTRUBTION STATEMENT A. APPROVED FOR PUBLIC RELEASE; DISTRIBUTION UNLIMITED.

13. SUPPLEMENTARY NOTES

This material is declared a work of the U.S. Government and is not subject to copyright protection in the United States.

14. ABSTRACT

Recent advancements in fiber laser technology have increased interest in target material interactions and the development of thermal protection layers for tactical laser defense. A significant material of interest is carbon fiber reinforced polymers due to their increased use in aircraft construction. In this work, the thermal response of carbon fiber-carbon nanotube (CNT) hybrid composites exposed to average irradiances of 0.87-6.8 W/cm^2 were observed using a FLIR sc6900 thermal camera. The camera had a pixel resolution of 640x512 which resulted in a spatial resolution of 0.394x0.383 mm/pixel for the front and 0.463x0.491 mm/pixel for the back. The hybrid samples that showed the highest absolute and relative reduction in heat penetration contained three CNT outer layers on the front and backside and one CNT center layer respectively. When compared to the 8-layer carbon fiber control sample, they demonstrated a backside peak temperature reduction of 120 ℃ and 85 ℃ respectively. This reduction in temperature appears to be due to the production of an insulating layer produced by the trapping of organic volatile gases in the CNT layers. The introduction of CNT layers to carbon fiber reinforced composites reduced heat penetration to deeper layers reducing subsequent thermal.

15. SUBJECT TERMS

Carbon Fiber, Carbon Nanotube, Laser Protection, Composites

16. SECURITY CLASSIFICATION OF:			**17. LIMITATION OF ABSTRACT**	**18. NUMBER OF PAGES**	**19a. NAME OF RESPONSIBLE PERSON** Maj Nicholas Herr, AFIT/ENP
a. REPORT	**b. ABSTRACT**	**c. THIS PAGE**			**19b. TELEPHONE NUMBER** *(Include area code)*
U	**U**	**U**	**UU**	107	(937)255-3636 x4524 nicholas.herr.1@us.af.mil

Standard Form 298 (Rev. 8-98)
Prescribed by ANSI Std. Z39-18